Article

A year-round satellite sea-ice thickness record from CryoSat-2

https://doi.org/10.1038/s41586-022-05058-5

Received: 8 November 2021

Accepted: 30 June 2022

Published online: 14 September 2022

Check for updates

Jack C. Landy[1,2]✉, Geoffrey J. Dawson[2], Michel Tsamados[3], Mitchell Bushuk[4], Julienne C. Stroeve[3,5], Stephen E. L. Howell[6], Thomas Krumpen[7], David G. Babb[5], Alexander S. Komarov[8], Harry D. B. S. Heorton[3], H. Jakob Belter[7] & Yevgeny Aksenov[9]

Arctic sea ice is diminishing with climate warming[1] at a rate unmatched for at least 1,000 years[2]. As the receding ice pack raises commercial interest in the Arctic[3], it has become more variable and mobile[4], which increases safety risks to maritime users[5]. Satellite observations of sea-ice thickness are currently unavailable during the crucial melt period from May to September, when they would be most valuable for applications such as seasonal forecasting[6], owing to major challenges in the processing of altimetry data[7]. Here we use deep learning and numerical simulations of the CryoSat-2 radar altimeter response to overcome these challenges and generate a pan-Arctic sea-ice thickness dataset for the Arctic melt period. CryoSat-2 observations capture the spatial and the temporal patterns of ice melting rates recorded by independent sensors and match the time series of sea-ice volume modelled by the Pan-Arctic Ice Ocean Modelling and Assimilation System reanalysis[8]. Between 2011 and 2020, Arctic sea-ice thickness was 1.87 ± 0.10 m at the start of the melting season in May and 0.82 ± 0.11 m by the end of the melting season in August. Our year-round sea-ice thickness record unlocks opportunities for understanding Arctic climate feedbacks on different timescales. For instance, sea-ice volume observations from the early summer may extend the lead time of skilful August–October sea-ice forecasts by several months, at the peak of the Arctic shipping season.

Sea-ice thickness (SIT) is an essential climate variable that shapes almost every physical and biogeochemical process operating at the Arctic air–ice–ocean interface. It guides human activities, as a platform for local Inuit communities to travel[3] and as a barrier and a key risk parameter for marine shipping[9]; it affects the amount of sunlight reaching ice-associated or under-ice primary producers[10], which make up the base of the entire Arctic food chain, particularly during summer months; and it helps to regulate the Arctic Ocean's biogeochemistry, including greenhouse gas fluxes[11]. Regional SIT anomalies tend to have a longer 'memory' (months) than sea-ice extent (SIE) anomalies (days), dictating where thicker-than-usual sea ice can survive summer melting or where thinner-than-usual sea ice melts away earlier in the season[12,13]. Consequently, SIT observations—particularly from the early summer[6]—have the potential to extend operational sea-ice forecasts by many months[14].

Pan-Arctic maps of winter SIT have been produced from a satellite radar and laser altimetry record spanning 1993 to the present[15–18], revealing that the sea-ice cover has been rapidly thinning in response to climate warming[19]. However, meltwater ponds accumulating on Arctic sea ice between May and September have prevented researchers from generating valid SIT observations in the summer months from any satellite sensor. This includes the European Space Agency (ESA) radar altimeter CryoSat-2, which has collected observations all year round since the mission was launched in 2010, but conventional algorithms have only enabled SIT to be derived for the winter months of October to April[17]. Melt ponds complicate the interpretation of CryoSat-2 radar data, so it is difficult to differentiate between sea-ice and the open-water leads that develop between sea-ice floes[20]. Furthermore, melt ponds bias the height measurement of the sea-ice surface elevation above the water level (that is, the ice freeboard), which is critical for estimating its thickness[7].

Summer SIT observations have been acquired on airborne campaigns and from in situ instruments such as moored sonar that record the sea-ice draft. These datasets have suggested that sea ice in the Arctic outflow region of Fram Strait has thinned by up to 50% since 2000[21] with a 25% decrease in the modal thickness of multi-year ice (MYI)[22], reflecting a strong decline in the age of sea ice surviving the summer melt in the Arctic Basin. However, airborne and in situ observations give only limited snapshots of the ice thickness for a single day or location.

Summer sea-ice thickness from CryoSat-2

In a recent study, deep learning was applied to CryoSat-2 radar returns to accurately distinguish sea-ice floes from leads, based on local variations

[1]Centre for Integrated Remote Sensing and Forecasting for Arctic Operations, Department of Physics and Technology, University of Tromsø The Arctic University of Norway, Tromsø, Norway. [2]Bristol Glaciology Centre, School of Geographical Sciences, University of Bristol, Bristol, UK. [3]Centre for Polar Observation and Modelling, Department of Earth Sciences, University College London, London, UK. [4]National Oceanic and Atmospheric Administration/Geophysical Fluid Dynamics Laboratory, Princeton, NJ, USA. [5]Centre for Earth Observation Science, University of Manitoba, Winnipeg, Manitoba, Canada. [6]Environment and Climate Change Canada, Climate Research Division, Toronto, Ontario, Canada. [7]Alfred Wegener Institute, Helmholtz Centre for Polar and Marine Research, Bremerhaven, Germany. [8]Environment and Climate Change Canada, Meteorological Research Division, Ottawa, Canada. [9]Marine Systems Modelling Group, National Oceanography Centre, Southampton, UK. ✉e-mail: jack.c.landy@uit.no

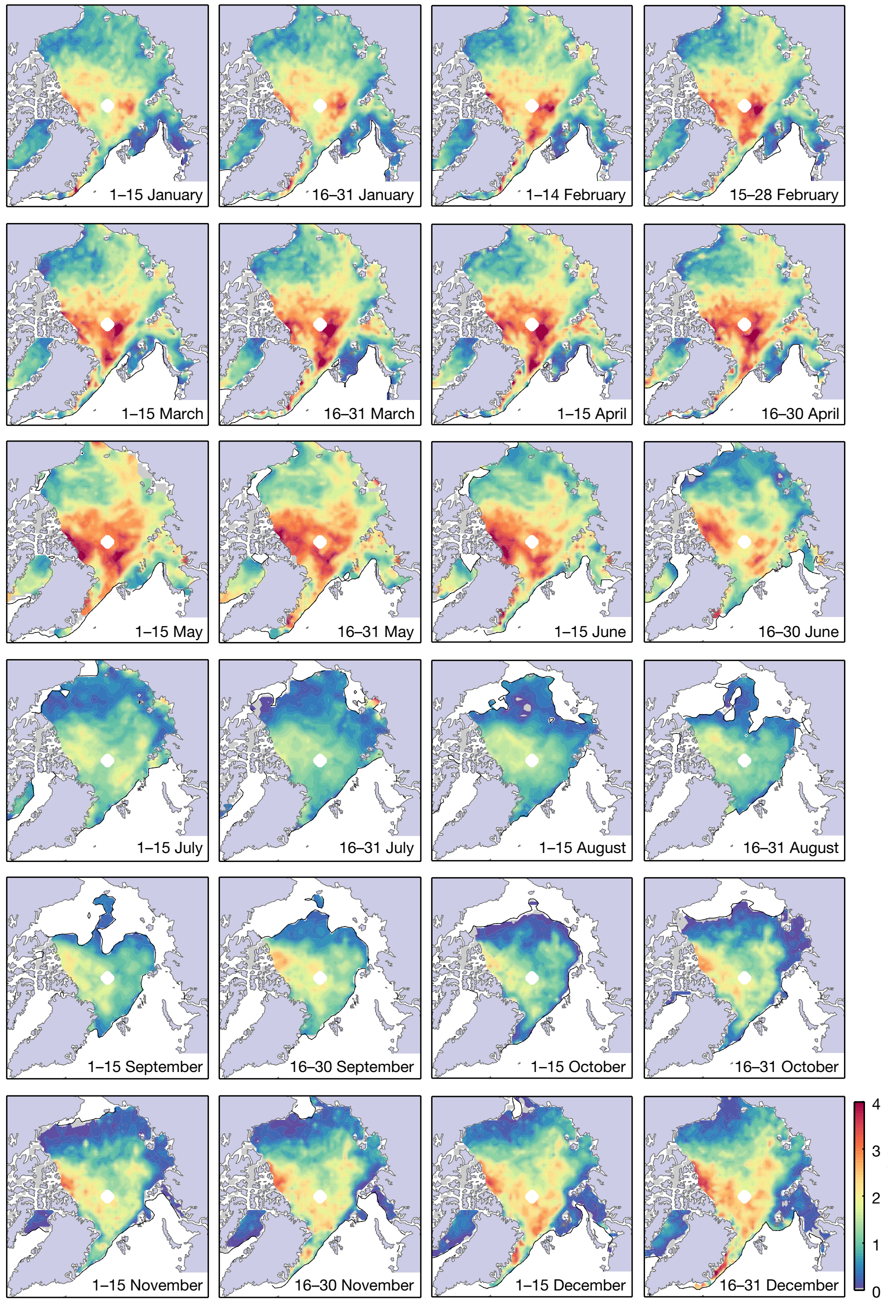

Fig. 1 | Arctic SIT measured over the entire year at biweekly (twice per month) intervals by CryoSat-2 in 2016. Observations for the cold-season months of October–April are obtained from the LARM algorithm[41]. Observations for the melting season months of May–September are obtained from the method presented here (Methods). The black contours represent the SIE (15% ice concentration edge) and greyed-out areas represent missing data. Maps produced using MATLAB code from ref. [42].

in the radar echo response, for the months of May to September[7]. The sea-ice radar freeboard was then determined from the elevation difference between altimeter measurements of sea-ice floes and the sea level at leads. CryoSat-2 radar freeboard measurements capture the patterns and timing of summer sea-ice melting rates observed by independent airborne and in situ 'ground truth' sensors; however, they underestimate the thickness of the thickest, roughest sea ice resident in the Central Arctic[7]. This is caused by an electromagnetic (EM) range bias on the CryoSat-2 radar measurement associated with meltwater ponds lying at the sea-ice surface.

Radar altimetry measurements of sea-ice freeboard rely on accurate detection of the mean level of ice floe surfaces. If the principal scattering horizon of the radar is not located at the same height as the mean ice floe surface height, the altimeter range measurement will be biased. Arctic sea-ice floe echoes are generally specular in the summer months[20] causing the waveform peak power to be referenced to the surface of reflecting ponds. Melt-pond surfaces typically lie below the mean elevation of the surrounding sea ice[23] causing a positive EM range bias over ice floes, which corresponds to an underestimation of the sea-ice freeboard. This positive EM range bias is larger over rougher sea ice[7], equivalent to the well understood sea-state bias over open ocean where Ku-band radar altimeter pulses are reflected more effectively by wave troughs than their crests[24].

Here we model the CryoSat-2 radar response over melt-pond-covered sea ice and perform a set of simulations to characterize the EM range

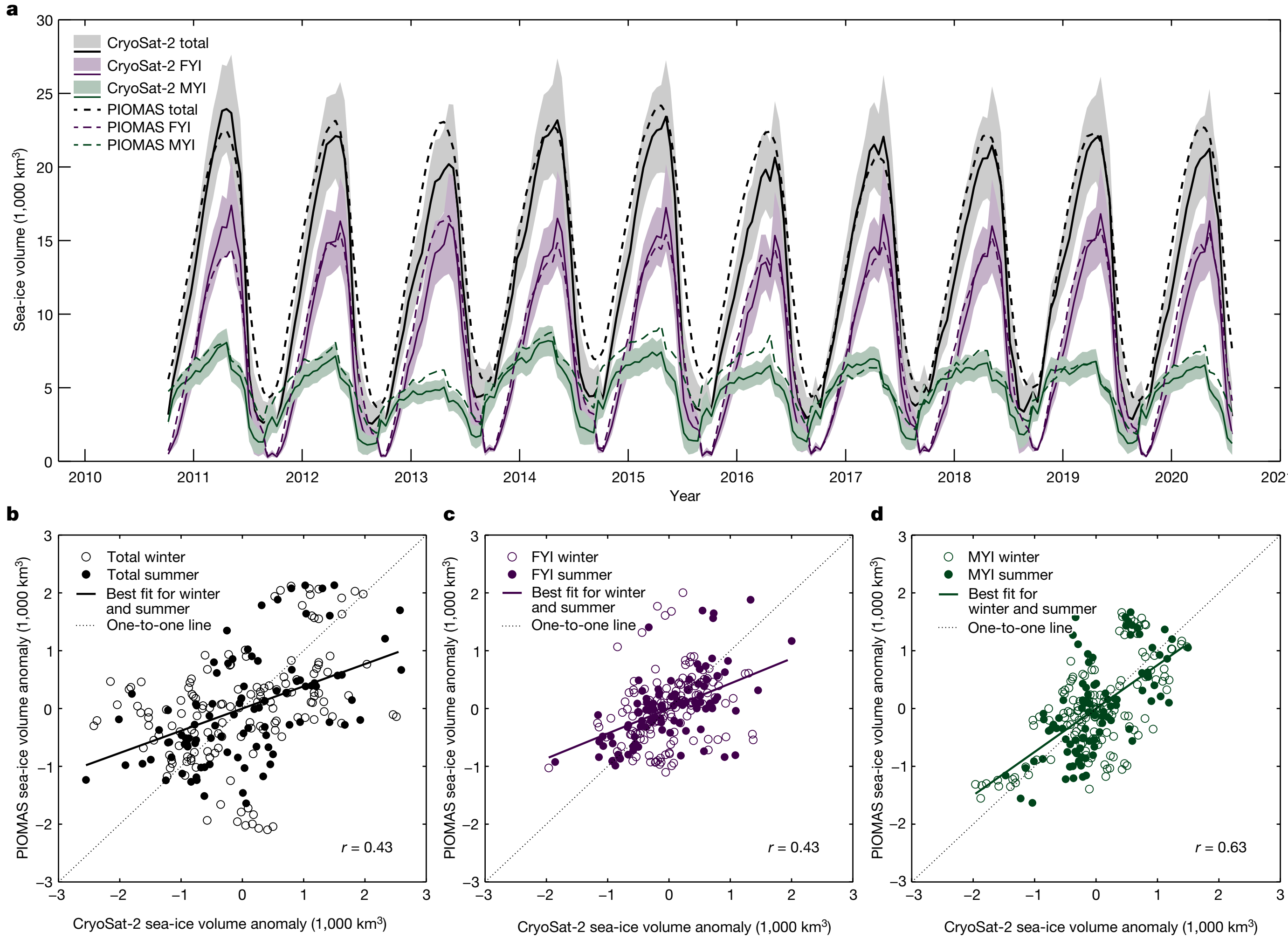

Fig. 2 | Time series of SIV derived from CryoSat-2 compared with reanalysed predictions of ice volume from PIOMAS. a, SIV from CryoSat-2 is presented with uncertainty envelopes for the entire Arctic and separated into zones of predominantly FYI and MYI (using the NSIDC sea-ice-age dataset[43]). The CryoSat-2 SIV uncertainties are derived from the total ice thickness uncertainty (Methods) multiplied by the ice area. **b**–**d**, Scatterplots of the SIV anomalies, for total (**b**), first-year (**c**) and multi-year (**d**) ice after removing the climatological seasonal cycle of ice volume from the CryoSat-2 and the PIOMAS time series.

bias (Methods). The simulations confirm that the radar range is increasingly overestimated as the sea-ice surface gets rougher, accounting for the observed underestimation of CryoSat-2 freeboard over rough sea ice in the Central Arctic[7]. We use auxiliary satellite estimates for the sea-ice surface roughness and melt-pond coverage during Arctic summer months to obtain a quantitative prediction for the EM range bias for every CryoSat-2 freeboard observation. The bias correction uncertainty is assessed through Monte Carlo error analysis. Estimates of snow loading on the sea ice (from snow depth and density) using a Lagrangian snow evolution scheme SnowModel-LG[25,26] are then used to convert the CryoSat-2 summer radar freeboards to SIT.

This approach enables us to create a pan-Arctic all-year, decade-long and gap-free SIT record for 2011–2020 (available with this paper). By doing so, we take steps towards a goal of the future European Union CRISTAL (Copernicus Polar Ice and Snow Topography Altimeter) mission to provide 'meaningful' SIT observations in summer[27]. The thickest pan-Arctic average SIT of 2.01 m was recorded in May 2015 whereas the thinnest SIT of 0.52 m was recorded in October 2011. The interannual variability of SIT across our 2011–2020 record is smallest at 0.08 m in January and largest at 0.18 m in July. In Fig. 1, we show, for example, biweekly (twice per month) 80-km resolution maps of SIT measured by CryoSat-2 over 2016. The record bridges two data-processing algorithms, for winter and summer months, but the spatial SIT distributions are generally consistent across the transitions from April to May and from September to October. For instance, in 2016, sea ice was thinner than usual in the Pacific sector of the Arctic, with a significant negative SIT anomaly appearing in February, growing to around 1 m by June (30% thinner than the 2011–2020 mean; Extended Data Fig. 6), and culminating in 7 weeks early ice-edge retreat in the Beaufort Sea[28].

Validating the ice thickness record

We have validated the satellite SIT observations against available airborne electromagnetic (AEM) sounding, upward-looking sonar (ULS) and acoustic Doppler current profiler (ADCP) observations acquired over the Arctic summer months. CryoSat-2 SIT can explain 80% of the variance (r^2) in coinciding helicopter-based AEM ice thickness observations collected during the 2011 TransArc campaign of the Alfred Wegener Institute (AWI) RV *Polarstern* icebreaker, verifying the gradient of SIT from the Central Arctic to the sea-ice edge recorded during TransArc (Extended Data Fig. 2). The distribution of SIT north of Greenland recorded by AEM during AWI IceBird campaigns from 2016 to 2018 is captured by CryoSat-2, although the satellite still underestimates the thickness of the roughest sea ice[29] in coastal areas (Extended Data

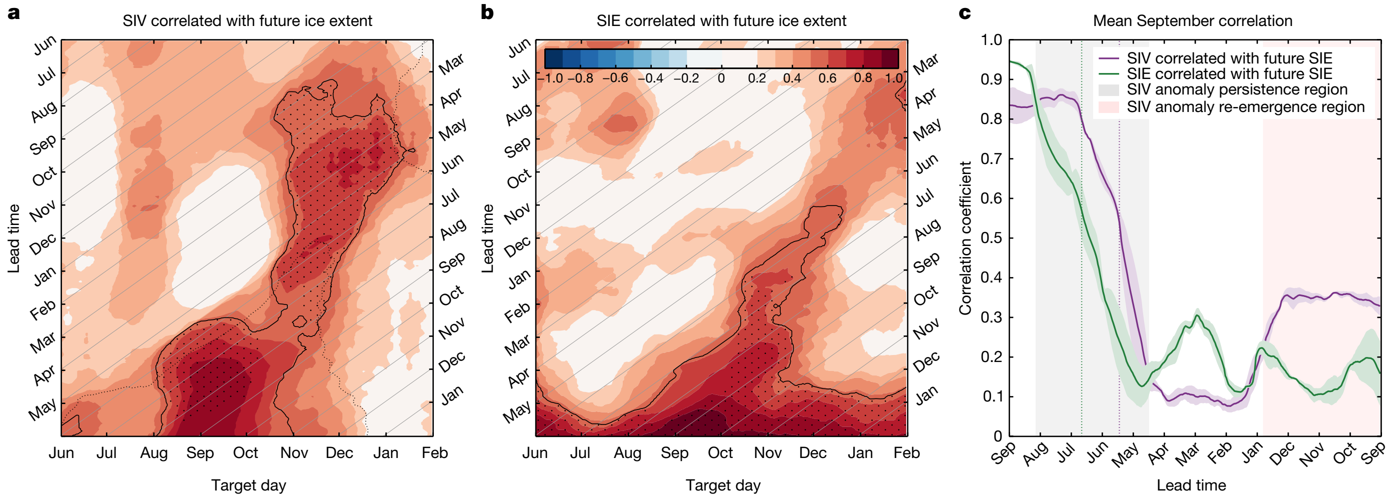

Fig. 3 | Lag correlation plots between pan-Arctic SIV and SIE. a,**b**, Correlations between SIV and future SIE (**a**) and correlations between SIE and future SIE (**b**). The black lines mark correlations with a statistical significance of $P = 0.1$ and stippling marks where SIV > SIE correlations are higher than SIE > SIE for **a** or vice versa for **b**. The dotted line in **a** marks the correlations with a significance of $P = 0.1$ between PIOMAS SIV and future OSISAF SIE. The grey lines mark lead times for each month as contours. The lagged correlation can be identified on the plot where SIV/SIE at any lead month on the *y* axis intersects with future SIE for any target month on the *x* axis. **c**, Mean (with standard deviation envelope) correlation for September SIE including two regions of predictability where SIV offers improvements over SIE. The two vertical lines mark the dates when correlations fall below $P = 0.1$. The same plot for detrended SIV and SIE time series is shown in Extended Data Fig. 8.

Fig. 3). This bias must be taken into account if the observations are used, for instance, in future data-assimilation experiments.

CryoSat-2 can likewise capture the timing and magnitude of ice melting rates recorded by ULS sensors on mooring arrays at the Beaufort Gyre Exploration Program (BGEP) between 2011 and 2018 (Extended Data Fig. 4) and ULS and ADCP sensors in the Laptev Sea between 2010 and 2015 (Extended Data Fig. 5). The satellite observations can explain 71% and 54% of the variance (r^2) in the ice draft measured by BGEP and the Laptev Sea arrays, respectively. Furthermore, after removing the climatological mean seasonal cycles of ice draft from the three long time series in the Beaufort Sea, the anomaly correlation coefficients between ULS and CryoSat-2 observations are 0.45, 0.51 and 0.37 for moorings A, B and D, respectively. This suggests that CryoSat-2 summer observations can capture a significant portion of the interannual variability in SIT recorded by moored ULS sensors.

Seasonal variability in sea-ice volume

Our SIT observations allow us to quantify sea-ice volume (SIV) throughout the melt season by integrating CryoSat-2 SIT with ice concentration observations from the Ocean and Sea Ice Satellite Application Facility (OSI SAF) (Methods). SIV anomalies are then obtained from the time series of pan-Arctic total SIV, by removing the 2010–2020 climatological seasonal cycle, and decomposed into the contributions from sea-ice concentration (SIC) and SIT anomalies (Extended Data Fig. 7). This analysis demonstrates that SIT anomalies provide the dominant contribution to SIV interannual variability, around five times higher than the absolute contribution from ice concentration anomalies. The correlations between SIV anomalies and the anomalies of SIT, SIC and their correlated component are 0.97, 0.27 and 0.21, respectively.

We use the Pan-Arctic Ice Ocean Modeling and Assimilation System (PIOMAS) SIV reanalysis system, which assimilates SIC and sea-surface-temperature data[8,30], as a benchmark for indirectly assessing our observations. SIV derived from CryoSat-2 shows remarkable consistency with PIOMAS (Fig. 2a); the PIOMAS SIV is generally within the observation uncertainty bounds, at the pan-Arctic scale and when separated into zones of predominantly first-year ice (FYI) and MYI. The strong correspondence between SIV time series from CryoSat-2 and PIOMAS are supported by r^2 values and root-mean-square errors of 0.95 (FYI, 0.96; MYI, 0.83) and 2,350 km^3 (FYI, 1,190 km^3; MYI, 1,200 km^3), respectively.

SIV is typically higher from PIOMAS than from CryoSat-2 around the September minimum. However, both the observations and reanalysis capture a reduction in MYI volume following the record Arctic SIE minimum in 2012 and rebound in 2014 following reduced ice melt and strong ice convergence during summer 2013[31]. The anomaly correlation coefficient between PIOMAS and CryoSat-2 is 0.43 (FYI, 0.43; MYI, 0.63) after removing the climatological mean seasonal cycles of SIV from both time series. Although CryoSat-2 SIT generally replicates the seasonal cycle and magnitude of SIV from PIOMAS, the interannual variations in ice volume between datasets are not identical and appear to agree better for MYI than for FYI (Fig. 2b–d). This could point to errors in the satellite observations of SIT and/or limitations in the model-based reanalysis system.

Covariance between ice volume and extent

To further evaluate the year-round satellite SIT record and verify that SIT anomalies persist through time rather than being obscured by uncertainties (biases or random noise), we perform a lagged correlation analysis between pan-Arctic SIV derived from CryoSat-2 and future pan-Arctic SIE from OSISAF (Fig. 3). Figure 3a shows correlation coefficients between pan-Arctic total SIV and SIE, separated by a lag time between 0 and 365 days, based on the full record of data between October 2010 and July 2020. (It is noted that sea ice within the National Snow and Ice Data Center (NSIDC) Multisensor Analyzed Sea Ice Extent (MASIE) Central Arctic region (Extended Data Fig. 9) is excluded from this analysis because the region has been perennially ice covered over our study period.) Time series for these correlations therefore correspond to 9–11 years of CryoSat-2 data, depending on the target day, and generally do not show statistically significant trends over such short records. For robustness, we repeat the same analysis but detrend the SIV and the SIE time series before calculating correlations (Extended Data Fig. 8); however, the major features of Fig. 3 remain. We compare to a reference analysis of lagged correlations between pan-Arctic total SIE and future SIE in Fig. 3b.

Figure 3 illustrates statistically significant ($P < 0.1$) positive correlations between summer (June–September) SIE and earlier ice volume and extent, starting from lead times between May and July. The lead times for significant correlations increase over summer, matching the structure revealed by numerous idealized and operational model sea-ice prediction experiments[6,12,13,32]. Our observational results therefore confirm the existence of a spring predictability barrier, as suggested by previous modelling studies[14,33]. Intense sea-ice dynamics and new ice growth in late winter can weaken the link between winter SIT anomalies and summer SIE[28], so that predictability is subdued until melt onset[14]. Strong correlations between SIV and future SIE develop only when the sea-ice-albedo feedback acts to enhance existing SIT anomalies at the onset of the Arctic melt season[34].

Future implications for forecasting

For target months in the Arctic summer, SIE co-varies strongly with future SIE at short lead times of around 0–45 days (Fig. 3b), whereas SIV takes over as the dominant source of skill for predicting ice extent between August and December over lead times of 45–300 days (Fig. 3a). For instance, SIV is the dominant source of skill for predicting September SIE at lead times of 25–140 days (Fig. 3c), which is generally consistent with operational sea-ice forecasting systems[12]. SIT anomalies in our year-round CryoSat-2 dataset must be larger than the observation uncertainties, because strong correlations between SIV and SIE bridge the transitions between conventional winter and new summer processing algorithms. As there are significant ($P < 0.1$) correlations between SIE in September and SIV over 3.5 months earlier, in mid-May, compared with only 2 months earlier in late June for SIE (Fig. 3c), new summer SIT observations may also be valuable in future to extend the lead time of Arctic sea-ice forecasts.

Our results further reveal the re-emergence of SIV as a potential source of skilful ice extent predictability in autumn months (Fig. 3a). The lead times for this re-emergence region are between 100 and 310 days, suggesting that October–December SIE can be accurately forecast from SIV measured by CryoSat-2 as early as the preceding January–February, but not after July–August. Correlations between SIV and SIE are more uncertain for this re-emergence region (Extended Data Fig. 10) and weaker—but still present—when time series are detrended (Extended Data Fig. 8). The skill is mainly sourced from the Beaufort, Chukchi and East Siberian seas where the sea ice can be less dynamic than in other regions (Extended Data Fig. 9). These results offer the exciting potential for SIT observations to enhance future sea-ice forecasts by bridging the spring and summer. For instance, CryoSat-2 SIV extends the lead time for skilful ice extent predictability in autumn by several months compared with using PIOMAS reanalysed SIV (Fig. 3a).

Autumn SIE predictions at lead times of up to around 200 days (Fig. 3a) can be explained by the persistence of early melt season SIT anomalies, whereas the correlations at lead times of less than 100 days are obscured by new ice formation in October and November. However, the skilful SIE forecasts at lead times of up to 280–310 days can only be explained by re-emergence of winter SIT anomalies in the following autumn. This could potentially occur through sequential hand-off from winter SIT anomalies to spring SIE anomalies to summer upper ocean heat anomalies to autumn SIE anomalies[33,35]. So-called growth-to-melt season re-emergence represents the exchange of anomalies between sea-ice area and thickness[12]. The two properties co-vary during summer but not in winter[35], with positive regional winter SIT anomalies slowing down sea-ice retreat in the following spring and creating positive summer SIE anomalies, or vice versa[36]. A shorter open-water season limits solar heating of the upper ocean, which extends this predictability regime through the melt-to-growth re-emergence mechanism[35]. Our observational results reinforce modelling studies that find SIV is a better predictor than SIE for July–November ice extent 6–10 months in advance[12].

Next steps

The pan-Arctic summer SIT product presented here could benefit from a number of improvements. Dedicated airborne campaigns to simultaneously measure the Ku-band radar response, surface roughness, freeboard and thickness of melt-pond-covered sea ice are required to better understand the EM radar range bias. The evolutions of FYI and MYI densities with summer brine drainage and meltwater flushing are poorly understood[37]. Gap-free and consistent satellite data products for Arctic summer melt-pond fraction and surface roughness are needed to improve the application of freeboard bias corrections. Finally, a greater emphasis on collecting SIT validation datasets during the Arctic summer—especially in the shoulder months of May and September—is essential for evaluating satellite products.

Future near-real time summer altimetry SIT observations could improve the safety of Arctic shipping through integration into the Polar Operational Limit Assessment Risk Index System (POLARIS)[38] that has been developed under the International Maritime Organization's Polar Code. Quantifying SIT, compared with qualitatively characterizing 'ice conditions' within the code, offers the critical information required to guide go or no-go decisions for Arctic vessels[5] and make future projections of Arctic navigation risks[9]. 'Missing' summer SIT observations have also impacted many fields of Arctic research beyond seasonal sea-ice forecasting. For instance, SIT is needed to close the energy budget of the Arctic Ocean during summer months[39]; to determine pelagic and sympagic primary productivity during the active summer bloom[10]; to reconcile the greenhouse gas balance of the Arctic[11]; and to validate and improve the representation of sea ice in global coupled climate models[40]. Our freely available summer SIT dataset opens research opportunities in all areas of Arctic-system science.

Online content

Any methods, additional references, Nature Research reporting summaries, source data, extended data, supplementary information, acknowledgements, peer review information; details of author contributions and competing interests; and statements of data and code availability are available at https://doi.org/10.1038/s41586-022-05058-5.

1. Notz, D. & Stroeve, J. Observed Arctic sea-ice loss directly follows anthropogenic CO_2 emission. *Science* **354**, 747–750 (2016).
2. Kinnard, C. et al. Reconstructed changes in Arctic sea ice over the past 1,450 years. *Nature* **479**, 509–512 (2011).
3. Eicken, H. Arctic sea ice needs better forecasts. *Nature* **497**, 431–433 (2013).
4. Kwok, R., Spreen, G. & Pang, S. Arctic sea ice circulation and drift speed: decadal trends and ocean currents. *J. Geophys. Res. Oceans* **118**, 2408–2425 (2013).
5. Mudryk, L. R. et al. Impact of 1, 2 and 4 °C of global warming on ship navigation in the Canadian Arctic. *Nat. Clim. Change* **11**, 673–679 (2021).
6. Bushuk, M. et al. Skillful regional prediction of Arctic sea ice on seasonal timescales. *Geophys. Res. Lett.* **44**, 4953–4964 (2017).
7. Dawson, G. et al. A 10-year record of Arctic summer sea ice freeboard from CryoSat-2. *Rem. Sens. Environ.* **268**, 112744 (2022).
8. Zhang, J. & Rothrock, D. A. Modeling global sea ice with a thickness and enthalpy distribution model in generalized curvilinear coordinates. *Mon. Weather Rev.* **131**, 845–861 (2003).
9. Aksenov, Y. et al. On the future navigability of Arctic sea routes: high-resolution projections of the Arctic Ocean and sea ice. *Mar. Policy* **75**, 300–317 (2017).
10. Stroeve, J. C. et al. A multi-sensor and modelling approach for mapping light under sea ice. *Front. Mar. Sci.* **7**, 592337 (2021).
11. Parmentier, F. J. W. et al. The impact of lower sea-ice extent on Arctic greenhouse-gas exchange. *Nat. Clim. Change* **3**, 195–202 (2013).
12. Guemas, V. et al. A review on Arctic sea-ice predictability and prediction on seasonal to decadal time-scales. *Q. J. R. Meterol. Soc.* **142**, 546–561 (2016).
13. Ordoñez, A. C., Bitz, C. M. & Blanchard-Wrigglesworth, E. Processes controlling Arctic and Antarctic sea ice predictability in the Community Earth System Model. *J. Clim.* **31**, 9771–9786 (2018).
14. Bushuk, M., Winton, M., Bonan, D. B., Blanchard-Wrigglesworth, E. & Delworth, T. A mechanism for the Arctic sea ice spring predictability barrier. *Geophys. Res. Lett.* **47**, e2020GL088335 (2020).
15. Laxon, S., Peacock, N. & Smith, D. High interannual variability of sea ice thickness in the Arctic region. *Nature* **425**, 947–950 (2003).
16. Kwok, R. & Cunningham, G. F. ICESat over Arctic sea ice: estimation of snow depth and ice thickness. *J. Geophys. Res.* **113**, C08010 (2008).

17. Laxon, S. W. et al. CryoSat-2 estimates of Arctic sea ice thickness and volume. *Geophys. Res. Lett.* **40**, 732–737 (2013).
18. Petty, A. A., Kurtz, N. T., Kwok, R., Markus, T. & Neumann, T. A. Winter Arctic sea ice thickness from ICESat-2 freeboards. *J. Geophys. Res. Oceans* **125**, e2019JC015764 (2020).
19. Kwok, R. Arctic sea ice thickness, volume, and multiyear ice coverage: losses and coupled variability (1958–2018). *Environ. Res. Lett.* **13**, 105005 (2018).
20. Kwok, R., Cunningham, G. F. & Armitage, T. W. K. Relationship between specular returns in CryoSat-2 data, surface albedo, and Arctic summer minimum ice extent. *Elementa* **6**, 53 (2018).
21. Renner, A. H. et al. Evidence of Arctic sea ice thinning from direct observations. *Geophys. Res. Lett.* **41**, 5029–5036 (2014).
22. Belter, H. J. et al. Interannual variability in transpolar drift summer sea ice thickness and potential impact of Atlantification. *Cryosphere* **15**, 2575–2591 (2021).
23. Eicken, H., Grenfell, T. C., Perovich, D. K., Richter-Menge, J. A. & Frey, K. Hydraulic controls of summer Arctic pack ice albedo. *J. Geophys. Res.* **109**, C08007 (2004).
24. Melville, W. K. et al. Measurements of electromagnetic bias in radar altimetry. *J. Geophys. Res. Oceans* **96**, 4915–4924 (1991).
25. Liston, G. E. et al. A Lagrangian snow-evolution system for sea-ice applications (SnowModel-LG): Part I—Model description. *J. Geophys. Res. Oceans* **125**, e2019JC015913 (2020).
26. Stroeve, J. et al. A Lagrangian snow evolution system for sea ice applications (SnowModel-LG): Part II—Analyses. *J. Geophys. Res. Oceans* **125**, e2019JC015900 (2020).
27. Kern, M. et al. The Copernicus Polar Ice and Snow Topography Altimeter (CRISTAL) high-priority candidate mission. *Cryosphere* **14**, 2235–2251 (2020).
28. Babb, D. G., Landy, J. C., Barber, D. G. & Galley, R. J. Winter sea ice export from the Beaufort Sea as a preconditioning mechanism for enhanced summer melt: a case study of 2016. *J. Geophys. Res.* **124**, 6575–6600 (2019).
29. Farrell, S. L., Duncan, K., Buckley, E. M., Richter-Menge, J. & Li, R. Mapping sea ice surface topography in high fidelity with ICESat-2. *Geophys. Res. Lett.* **47**, e2020GL090708 (2020).
30. Schweiger, A. et al. Uncertainty in modeled Arctic sea ice volume. *J. Geophys. Res.* **116**, C00D06 (2011).
31. Kwok, R. Sea ice convergence along the Arctic coasts of Greenland and the Canadian Arctic Archipelago: variability and extremes (1992–2014). *Geophys. Res. Lett.* **42**, 7598–7605 (2015).
32. Bonan, D. B., Bushuk, M. & Winton, M. A spring barrier for regional predictions of summer Arctic sea ice. *Geophys. Res. Lett.* **46**, 5937–5947 (2019).
33. Day, J. J., Hawkins, E. & Tietsche, S. Will Arctic sea ice thickness initialization improve seasonal forecast skill? *Geophys. Res. Lett.* **41**, 7566–7575 (2014).
34. Schröder, D., Feltham, D. L., Flocco, D. & Tsamados, M. September Arctic sea-ice minimum predicted by spring melt-pond fraction. *Nat. Clim. Change* **4**, 353–357 (2014).
35. Blanchard-Wrigglesworth, E., Armour, K. C., Bitz, C. M. & DeWeaver, E. Persistence and inherent predictability of Arctic sea ice in a GCM ensemble and observations. *J. Clim.* **24**, 231–250 (2011).
36. Chevallier, M. & Salas-Mélia, D. The role of sea ice thickness distribution in the Arctic sea ice potential predictability: a diagnostic approach with a coupled GCM. *J. Clim.* **25**, 3025–3038 (2012).
37. Eicken, H. et al. Thickness, structure, and properties of level summer multiyear ice in the Eurasian sector of the Arctic Ocean. *J. Geophys. Res. Oceans* **100**, 22697–22710 (1995).
38. Stoddard, M. A., Etienne, L., Fournier, M., Pelot, R. & Beveridge, L. Making sense of arctic maritime traffic using the polar operational limits assessment risk indexing system (POLARIS). *IOP Conf. Ser. Earth Environ. Sci.* **34**, 012034 (2016).
39. Perovich, D., Light, B. & Dickinson, S. Changing ice and changing light: trends in solar heat input to the upper Arctic ocean from 1988 to 2014. *Ann. Glaciol.* **61**, 401–407 (2020).
40. Schröder, D., Feltham, D. L., Tsamados, M., Ridout, A. & Tilling, R. New insight from CryoSat-2 sea ice thickness for sea ice modelling. *Cryosphere* **13**, 125–139 (2019).
41. Landy, J. C., Petty, A. A., Tsamados, M. & Stroeve, J. C. Sea ice roughness overlooked as a key source of uncertainty in CryoSat-2 ice freeboard retrievals. *J. Geophys. Res. Oceans* **125**, e2019JC015820 (2020).
42. Roberts, A. ncpolarm (https://www.mathworks.com/matlabcentral/fileexchange/30414-ncpolarm). MATLAB Central File Exchange (2022).
43. Tschudi, M., Meier, W. N., Stewart, J. S., Fowler, C. & Maslanik, J. Polar Pathfinder Daily 25 km EASE-Grid Sea Ice Motion Vectors, Version 4. NASA National Snow and Ice Data Center Distributed Active Archive Center (2019).

Methods

CryoSat-2 sea-ice radar freeboards

SIT observations are derived from the ESA CryoSat-2 radar altimeter[44] following the processing chain illustrated in Extended Data Fig. 1. The first step of this method, documenting a record of sea-ice radar freeboard measurements obtained from CryoSat-2 over the Arctic summer 'melt season' months of May–September 2011–2020, has already been published[7]. The algorithm to obtain radar freeboard involved several steps. (1) Fitting the SAMOSA+ (Synthetic Aperture Radar Altimetry MOde Studies and Applications +) analytical radar echo model[45] to observed waveforms to retrack the ice or ocean surface elevation. Model fitting was performed using the ESA Grid Processing On Demand (GPOD) SARvatore and SARInvatore services. (2) Classification of radar waveforms into returns from sea-ice floes and leads using a one-dimensional convolutional neural network (CNN). The CNN was trained using CryoSat-2 samples selected over known surface types (sea-ice floes or leads) identified in coincident satellite optical and SAR imagery, as described in ref. [7]. (3) Finding the height difference between ice floe elevations and sea level. (4) Sampling the CryoSat-2 along-track radar freeboards to biweekly, 80-km-resolution grids through inverse distance- and time-weighted linear interpolation.

Hereafter, this section describes new techniques, building on ref. [7], to (1) characterize and correct for the EM range bias on CryoSat-2 radar freeboard observations, (2) convert freeboards to estimates of SIT with associated uncertainties, (3) reconcile summer and winter SIT records, (4) validate SIT observations, and (5) perform lagged correlation analyses between SIE and SIV.

Characterization of the EM range bias

Ideally, we would correct for the EM range bias over melt-pond-covered sea-ice floes at the radar waveform retracking step. However it would be extremely challenging—potentially impossible—to invert for the EM range bias correction solely from the shape of a CryoSat-2 waveform. Consequently, we estimate the EM bias separately then apply it as a correction to the biweekly 80-km radar freeboard product derived in ref. [7]. The radar range bias is quantified by comparing a set of numerical waveform simulations from sea-ice surfaces with the Facet-Based Echo Model (FBEM)[41,46], which integrates melt ponds, to solutions from the SAMOSA+ analytical echo model used for waveform retracking. Full details of the rationale for this approach, the waveform simulations and the bias quantification are given in Supplementary Section A and refs. [47–52].

We simulate the backscattered CryoSat-2 radar response with the FBEM from random sea-ice surfaces generated with a prescribed roughness height standard deviation σ and randomly distributed melt-pond coverage f_p. Melt ponds are distributed by accumulating water on the topography below a threshold elevation until the coverage equals f_p, with all pond surfaces sitting at the same elevation. Relevant parameters for modelling the sea-ice surface backscattering coefficients are obtained from the literature, including 'radar scale' (millimetre to centimetre) melt-pond surface roughness parameters based on field observations of melt-pond wave spectra[53]. Melt-pond surface roughness varies as a function of the wind speed U_{10}, so we run simulations with FBEM covering a wind speed range from 5 m s^{-1} to 7 m s^{-1} to characterize the uncertainty of this parameter. A look-up table of altimeter echoes is generated from the average of 100 model outputs for each combination of σ from 0 cm to 60 cm in 2-cm intervals and f_p from 0 to 0.6 in 0.02 intervals. As each model run is based on a randomly generated surface, we have to average 100 model outputs to accurately characterize the echo for a certain combination of σ and f_p.

The numerical FBEM simulations from pond-covered sea ice are assumed to represent 'true' radar echoes for certain combinations of σ and f_p, and then used as a reference for evaluating the SAMOSA+ retracking algorithm applied in our CryoSat-2 radar freeboard processing scheme[7]. We find the best-fit SAMOSA+ model solution for each FBEM echo in the look-up table, with the EM range bias then defined as the two-way travel time difference between echo retracking points. This produces a theoretical quantitative estimate for the EM range bias as a two-dimensional function of σ and f_p, which can then be applied as a correction on the CryoSat-2-derived radar freeboard.

Auxiliary estimates for the sea-ice surface roughness and melt-pond coverage during Arctic summer months are required to apply the theoretical range bias correction. At the time of writing, there is no consistent pan-Arctic gap-free dataset available for either parameter covering the study period from 2011 to 2020. We obtain pan-Arctic sea-ice surface roughness observations for summer months by propagating CryoSat-2 estimates of σ from the 25-km gridded Lognormal Altimeter Retracker Model (LARM) dataset[41] forwards and backwards from winter months, based on observations of the sea-ice drift. These roughness observations are assumed to represent the standard deviation of the snow–sea-ice interface. Daily observations of sea-ice drift are obtained from the NSIDC Polar Pathfinder dataset (https://nsidc.org/data/nsidc-0116/versions/4)[43]. A single estimate of σ is derived for each biweekly 80-km CryoSat-2 freeboard grid, between May and September, by sampling the inverse-time-weighted average of evolved Lagrangian April and October σ fields at each grid point. We estimate uncertainty on the roughness from the root sum square of the measurement uncertainty and the absolute difference between forwards and backwards predictions.

Remotely sensed observations of melt-pond fraction are obtained from the Sentinel-3 Ocean and Land Colour Instrument (OLCI) sensor through the University of Bremen (https://seaice.uni-bremen.de/melt-ponds/). This is a daily 12.5-km pan-Arctic product based on the version 1.5 algorithm of ref. [54] and covering the period between 2017 and 2020. As cloud cover can heavily obscure the coverage of daily observations and only the final four years of our freeboard record had coinciding measurements of f_p, we calculate a seasonal climatology of the f_p observations that we could then apply to all years of our study, 2011–2020. Biweekly 80-km melt-pond fraction fields are obtained from the average of all cloud-free OLCI pixels between 2017 and 2020 within each two-week summer window and 80-km grid cell. The f_p climatology captures the expected seasonal cycle of melt-pond formation, growth and drainage[23], and regional patterns in coverage reflecting the pan-Arctic differences between sea-ice types[55]. However, it does not account for interannual variations in f_p within the same region, which can be significant[56], and represent an uncertainty on our observations. We estimate the uncertainty on our melt-pond climatology from the root sum square of the f_p pixel standard deviation and the interannual variability of f_p between years of the 2017–2020 record.

The EM range bias correction Δh_r is calculated from inputs of σ from CryoSat-2 and f_p from Sentinel-3 OLCI, and then added to the CryoSat-2 radar freeboard estimates. This correction is not applicable when a significant snowpack is present on the sea-ice surface, so that melt-pond coverage would be limited. Therefore, we do not apply the correction when snow depth (see below) $h_s > 60$ cm and reduce the correction linearly as a function of snow depth between 0 cm and 60 cm (that is, $\Delta h_r \times (1 - h_s/60)$).

Uncertainty on the bias correction is assessed through Monte Carlo error analysis. For each value of the EM range bias, we have estimates for the uncertainties of three input parameters: σ, f_p, and the radar-scale melt-pond roughness induced by variable wind speed U_{10}. We recalculate the bias 1,000 times but each time including randomly selected errors from the error distributions of σ, f_p and U_{10}, obtaining the total uncertainty from the standard deviation of these 1,000 iterations. We assume that σ and f_p have Gaussian-distributed errors with standard deviations equal to the parameter uncertainties, but that radar-scale melt-pond roughness values are equally likely over the modelled range of U_{10} between 5 m s^{-1} and 7 m s^{-1}. The final uncertainty of the bias-corrected CryoSat-2 radar freeboard is obtained from the root sum square of the uncertainty on the EM bias correction and the measured freeboard variability within each 80-km grid cell. The uncertainty is highest (up to around 40% of the corrected freeboard) between July and August when the EM range bias correction is largest.

SIT and uncertainty

Snow load (depth and density) estimates are obtained from the Lagrangian snow evolution scheme SnowModel-LG[25,26]. This scheme uses the Modern-Era Retrospective analysis for Research and Applications Version 2 (MERRA2) atmospheric reanalysis and NSIDC Polar Pathfinder ice-motion observations to simulate the accumulation of snow on Arctic sea ice between September and April, while also modelling snowpack metamorphism and melt between May and August. Snow carryover between accumulation seasons is minimal and the snow melting season is around 6 weeks in length[25]. Snow melt occurs between May and July but is most rapid in June, reflecting the transition from a negative to positive Arctic surface-energy balance, before the snow accumulates again slowly from September. SnowModel-LG can reproduce the timing of snow melt from in situ observations but has difficulty predicting rates of melt[26]. We assume relatively high constant uncertainties in snow depth and density of 10 cm and 50 kg m^{-3}, respectively (or 50% if the depth or density are below these values). These uncertainties are based on the comparisons between SnowModel-LG data and those from independent datasets, including Operation IceBridge, ice mass balance buoys, snow buoys and MagnaProbes[26].

CryoSat-2 radar freeboards show clear unrealistic thickening between April and May[7] resulting from the radar signal attenuating within the melting snowpack[57] rather than penetrating to the snow–ice interface. This probably results from increasing moisture content within the snowpack causing scattering and absorption of the CryoSat-2 Ku-band EM wave. The depth of radar penetration into the snow will vary between regions, years and potentially from observation to observation along the satellite track, depending on the snow geophysical properties (roughness, microstructure, density, volume and salinity) and atmospheric conditions (temperature, moisture content and so on)[57–60]. As we cannot predict these variations in the penetration depth, as a first approximation we assume the Ku-band radar penetrates a constant 90% of the snow cover wherever snow is present between May and September, which produces a largely consistent transition in derived SIT between April and May, and between September and October. However, the assumed Ku-band radar penetration depth into snow during the Arctic melting season does impact the estimated SIT (Supplementary Section B) and should therefore be the subject of further study.

Sea-ice thickness h_i is obtained from the hydrostatic equation, accounting for snow loading above the radar penetration depth fraction δ_p and for the different densities of snow and sea ice below it as follows

$$h_i = \frac{h_s\rho_w - h_f\rho_w - h_s\rho_s - \delta_p h_s\rho_w}{\rho_i - \rho_w} \tag{1}$$

where h_f is the sea-ice freeboard, ρ_w, ρ_s and ρ_i are the densities of ocean water, snow and sea ice, respectively, and h_s is the snow depth. δ_p is the mean radar penetration expressed as a fraction of the snow depth, which here we assume is equal to 0.9. We apply the following function adapted from ref. [61] to correct for delayed radar wave propagation through the snowpack and convert from bias-corrected measured radar freeboard h_{rf} to bias-corrected sea-ice freeboard

$$h_f = h_{rf} + \delta_p h_s((1 + 0.51\rho_s/1,000)^{1.5} - 1) \tag{2}$$

(It is noted that we use the term 'measured' radar freeboard because we are not assuming that the measured radar freeboard coincides with the actual radar freeboard of the snow–ice interface).

The ocean water density ρ_w is assumed to be 1,024 kg m^{-3}. The sea-ice density is assumed to be 917 kg m^{-3} and 882 kg m^{-3} for FYI and MYI, respectively, following ref. [62]. We use the NSIDC weekly 12.5-km sea-ice-age product V4 (https://nsidc.org/data/nsidc-0611) to differentiate between zones of FYI and MYI. Constant sea-ice-type-dependent densities are used here to maintain consistency with CryoSat-2 SIT processing in cold-season months[63]; however, we can expect ice densities to vary significantly over the course of the summer melting season[37] and between regions[62]. Uncertainty on the sea-ice density is assumed to be 35.7 kg m^{-3} for FYI and 23.0 kg m^{-3} for MYI, multiplied by $1/\sqrt{N}$ with N the number of individual CryoSat-2 freeboard observations in an 80-km grid cell, following previous studies[63]. Snow depths and densities are from SnowModel-LG.

An example for the annual Arctic Ocean SIT evolution in 2016 is shown in Fig. 1, incorporating cold-season observations from the LARM algorithm[41] and melt-season observations from our method described here. The SIT data for winter months (October–April) are an updated ESA Baseline-D version of the Baseline-C dataset (available at https://data.bas.ac.uk/full-record.php?id=GB/NERC/BAS/PDC/01257). The LARM algorithm accounts for variable sea-ice surface roughness and backscattering properties[46], to derive radar freeboard for Arctic winter months[41]. We discuss the consistency between winter and summer SIT records below.

Uncertainty on the SIT is estimated from the individual uncertainties ε on four parameters: h_f, h_s, ρ_s and ρ_i, at the 80-km grid scale of the thickness observations. Assuming uncertainties between these variables are uncorrelated at 80-km scale, the total random thickness error ε_{h_i} is determined by Gaussian propagation of uncertainty as:

$$\varepsilon_{h_i}^2 = \left(\frac{\partial h_i}{\partial h_f}\varepsilon_{h_f}\right)^2 + \left(\frac{\partial h_i}{\partial h_s}\varepsilon_{h_s}\right)^2 + \left(\frac{\partial h_i}{\partial \rho_s}\varepsilon_{\rho_s}\right)^2 + \left(\frac{\partial h_i}{\partial \rho_i}\varepsilon_{\rho_i}\right)^2 \tag{3}$$

where the partial derivatives of equation (3) are used as weights for the variances of individual parameters to obtain their contribution to the ice thickness uncertainty:

$$\begin{aligned}
\frac{\partial h_i}{\partial h_f} &= \frac{\rho_w}{\rho_w - \rho_i}\\
\frac{\partial h_i}{\partial h_s} &= \frac{\rho_w - \rho_s - \delta_p\rho_w}{\rho_i - \rho_w}\\
\frac{\partial h_i}{\partial \rho_s} &= \frac{h_s}{\rho_w - \rho_i}\\
\frac{\partial h_i}{\partial \rho_i} &= \frac{h_f\rho_w + h_s\rho_s - h_s\rho_w + \delta_p h_s\rho_w}{(\rho_w - \rho_i)^2}
\end{aligned} \tag{4}$$

Median ice thickness uncertainty for summer months is estimated to be 33% of the thickness for FYI and 40% for MYI. Of this, the freeboard uncertainty dominates, contributing 80–90% of the total thickness uncertainty, with the snow depth then sea-ice density uncertainties contributing most of the remaining 10–20%.

Reconciling summer and winter CryoSat-2 SIT records

The algorithms for generating SIT observations from CryoSat-2 vary between summer (May–September) and winter (October–April) conditions. We use many of the same steps in both processing algorithms, including the same SnowModel-LG snow depth and density product, the same constant sea-ice densities for FYI and MYI, and the same method for uncertainty propagation; however, other steps are necessarily different. To evaluate the consistency between these datasets, we examine the transitions in ice thickness and thickness anomalies across the 'shoulder' months of April–May and September–October. Figure 2 illustrates that SIV from CryoSat-2 typically varies smoothly across the shoulder months. Only in a few years (2014 at mooring B and 2017 at mooring D) does the CryoSat-2 time series of sea-ice draft appear to jump between April and May in the Beaufort Sea (Extended Data Fig. 4).

The patterns of SIT shown in Fig. 1 do not change appreciably across the shoulder months, with the exception of new thin sea ice in the marginal ice zone at the end of September, which appears to be overestimated compared with the same locations in early October. Thin-ice retrieval is a known limitation of the summer radar freeboard algorithm[7].

Importantly, SIT anomalies persist from winter to summer and back to winter months at the same locations, which we would not expect to see if uncertainty exceeded the CryoSat-2 ice thickness signal. For instance, a negative SIT anomaly appears in the Pacific sector of the Arctic in February 2016, grows to >1 m (about 30% thinner than the 2011–2020 average) by May–June, before sea ice in the Beaufort Sea broke up and melted away completely 7 weeks earlier than usual in August (Extended Data Fig. 6). Reference [28] showed that anomalously high sea-ice export and divergence promoted the formation of thin ice between February and April that preconditioned sea ice in the Beaufort Sea for early break up and only the second ice-free Beaufort Sea on record. This a perfect example of the regional 'growth-to-melt season re-emergence' discussed in the main text and now measurable by our summer CryoSat-2 thickness product. By contrast, a positive SIT anomaly appears in the Kara Sea in June (Extended Data Fig. 6) and persists through summer into the following sea-ice growth season, leading to >1-m-thicker sea ice than usual in this region by the end of 2016.

Validation against independent datasets

Gridded CryoSat-2 SIT observations are validated against independent measurements of SIT from AEM induction datasets[22,64] from the Central Arctic Ocean and Lincoln Sea, and sea-ice draft from mooring ULS arrays in the Beaufort and Laptev seas, and in Fram Strait. All validations are presented here.

AEM data. The AEM dataset includes observations from the AWI RV *Polarstern* ARK-XXVI/3 TransArc campaign in 2011[64] (available from https://doi.org/10.1594/PANGAEA.937197) and the IceBird campaigns from 2016 to 2018[22]. For the TransArc campaign, the sensor was attached to a helicopter and collected ice thickness observations over small surveys around RV *Polarstern* in the Central Arctic Ocean (Extended Data Fig. 2) between August and September. In the IceBird campaigns, the sensor was towed by a fixed-wing aircraft and collected ice thickness observations over large surveys covering the coast of Northern Greenland and the Fram Strait in late July and August (Extended Data Fig. 3). The AEM sensor estimates SIT by measuring the electrical conductivity difference between ice and ocean water and is estimated to have an uncertainty of ±0.1 m over level ice[65] but the accuracy can be reduced in the presence of melt ponds[66]. The airborne observations have a footprint on the scale of tens of metres, so we average them to 80 km before comparing with CryoSat-2.

The CryoSat-2 observations in August–September 2011 match very closely to the AEM data acquired on TransArc. They can explain 80% of the variance in the AEM data, with a mean difference of −16 cm (CryoSat-2 minus AEM) and a root-mean-square error of only 13 cm (Extended Data Fig. 2). Satellite data mostly capture the range in average thickness between the Central Arctic MYI pack ice in August (1–1.5 m) and the decayed and melting FYI closer to the margins in September (<1 m). However, the slope between CryoSat-2 and air EM SIT measurements is 0.72, so CryoSat-2 does not quite match the full dynamic range of thickness acquired by the helicopter.

The CryoSat-2 observations from 2016 to 2018 underestimate the AEM SIT observations collected on IceBird campaigns, with a median difference of 28 cm (Extended Data Fig. 3). However, by calculating the CryoSat-2 SIT without correcting for the roughness-induced EM range bias, the median difference increases to 82 cm. The EM range bias for CryoSat-2 is highest over the roughest sea ice in the Lincoln Sea and above Northern Greenland, so it is most crucial to apply a correction in this region. There is a clear relationship between the mean CryoSat-2 and AEM ice thickness difference and the distance from the nearest coastline (Extended Data Fig. 3c). CryoSat-2 underestimates the AEM ice thickness most severely within 150 km of the coast, whereas there is a very low mean difference at distances >150 km from the coastline. This suggests there is still a roughness bias remaining for the heavily deformed sea ice in coastal locations[29].

ULS data. The BGEP moorings have been maintained in the Beaufort Sea since 2003, monitoring freshwater and heat content in the Arctic Ocean, including the solid freshwater flux through observations of sea-ice draft. ULS ice draft observations from moorings A, B and D are available at https://www.whoi.edu/beaufortgyre for the period between 2011 and 2018 coinciding with our CryoSat-2 SIT observations. Furthermore, ULS and ADCP ice draft observations have been acquired at five moorings operated by AWI on the opposite side of the Arctic, in the Laptev Sea, and are publicly available at https://doi.org/10.1594/PANGAEA.899275 and https://doi.org/10.1594/PANGAEA.912927. Four of these moorings are located far enough away from the coast, with data acquired between 2010 and 2016, to be compared with CryoSat-2 SIT observations[67]. Each ULS ice draft observation is estimated to have an uncertainty of ±0.05–0.10 m (ref. [68]) whereas each ADCP ice draft is estimated to have a much higher uncertainty of around ±0.95 m (ref. [69]); however, the uncertainties are reduced by averaging data over time. Finally, ULS ice draft observations have been acquired at four moorings in Fram Strait from 1990 to 2018 and monthly averages are publicly available at https://doi.org/10.21334/npolar.2021.5b717274. The comparisons with CryoSat-2 enable us to validate the magnitude and timing of sea-ice melting rates obtained from our new year-round SIT product.

The sea-ice drafts are obtained from CryoSat-2 thickness data by removing the ice freeboard. Satellite-derived ice drafts from a radius of 150 km around each mooring are compared against a 31-day rolling average of daily measurements of the mean ice draft from the mooring ULS and ADCP sensors in Extended Data Figs. 4 and 5.

The mean bias and standard deviation on the bias are −16 ± 32 cm, −19 ± 34 cm and −27 ± 42 cm, for BGEP moorings A, B and D, respectively (CryoSat-2 minus ULS). Notably, the slope of the CryoSat-2-ULS comparison of 0.69 is very similar to the slope on the CryoSat-2-AEM comparisons made for TransArc (Extended Data Fig. 2). The correlations between the CryoSat-2 and ULS observations are 0.87, 0.84 and 0.85 for moorings A, B and D, respectively. If we just use a simple sea-ice-density-dependent freeboard-to-draft conversion, and a relatively high sea-ice density of 930 kg m^{-3}, without correcting for the EM range bias on freeboards or for snow loading, the correlation is only 0.66 and mean difference is −26 ± 50 cm (ref. [7]). By accounting for the range bias and snow loading in the ice freeboard-to-draft conversion, in this study, the correlation is improved by 30%, offset is reduced by 23% and variability reduced by 28%. The validity of our corrections for the EM range bias and snow loading are strongly supported by these improved validation statistics.

The mean bias and standard deviation on the bias is −6 ± 40 cm for the Laptev Sea moorings (CryoSat-2 minus ULS/ADCP). The average correlation between the CryoSat-2 and ULS/ADCP observations is 0.74. It is notable that mooring observations from the central Laptev Sea (Kotelny, Outer Shelf and 1893) match the CryoSat-2 SIT observations better than those from the western Laptev Sea (Vilk) (Extended Data Fig. 5). The central sites are less influenced by dynamics and sea-ice deformation, meaning that the ice cover is consistent and the higher uncertainty ADCP observations therefore have less impact. A previous comparison of these observations with a different CryoSat-2 SIT product for only winter months found greater mismatch when the mean and modal ice drafts were very different[67], which is a sign of strong ice deformation. This is the case for Vilk1 and Vilk3 in 2016 when the seasonal cycle of SIT had a very unusual shape (Extended Data Fig. 5).

The mean bias is +11 cm for the Fram Strait moorings (CryoSat-2 minus ULS) when including all valid observations from winter and summer months. However, the CryoSat-2 ice draft estimates are not available when SICs are below 70%, which is often the case over the Fram Strait moorings during summer. Therefore, we cannot reliably use the Fram Strait ULS data for validating the new CryoSat-2 summer SIT product.

Sea-ice volume

Before estimating SIV from the CryoSat-2 summer ice thickness observations, we fill spatial gaps in the thickness fields (where no valid CryoSat-2 freeboard observations are available) by two methods. Within the marginal ice zone, which is here defined as the area with SIC >15% and <60%, grid cells missing valid freeboard observations but containing strongly specular radar returns are assumed to characterize mainly thin, heavily pond-covered and decayed sea-ice floes[20]. These grid cells are defined where the backscatter coefficient is >40 dB, the range integrated power peakiness[7] is >25 or the pulse peakiness is >0.3. To these cells, we assign a thickness from the 5th percentile of the pan-Arctic ice thickness distribution for that time interval and an uncertainty of 50%. We use this method because the thickness in these marginal grid cells cannot be reliably interpolated from adjacent cells that may contain much thicker ice. However, only a small number of gaps are filled in this way, for instance, four or five grid cells per biweekly time slice in 2016. Remaining gaps within the main ice pack (ice concentrations >60%) are filled by linear interpolation from up to eight adjacent grid cells. (It is noted that the data product provided with this paper includes two thickness fields both omitting and including these gap-filled grid cells.)

SIV is then obtained from the ice thickness grids multiplied by SIC from the OSI SAF 'OSI-450' climate data record (available from https://osi-saf.eumetsat.int/products/osi-450[70]) and the grid-cell area. CryoSat-2-derived SIV is compared with the Applied Physics Laboratory Version 2.1 reprocessed PIOMAS ice volume data[8,30], using the NSIDC Sea Ice Age, Version 4 dataset[43] to separate zones of predominantly FYI and MYI. The domains are matched by comparing gridded SIV observations to the native PIOMAS grid and removing all non-overlapping data. SIV anomalies, SIV′, are obtained from the time series of pan-Arctic SIV by removing the 2010–2020 climatological seasonal cycle. The SIV anomalies are decomposed as follows

$$\mathrm{SIV}' = \int_A (\mathrm{SIC}'\overline{\mathrm{SIT}} + \overline{\mathrm{SIC}}\mathrm{SIT}' + \mathrm{SIC}'\mathrm{SIT}')\,\mathrm{d}A \qquad (5)$$

where bars represent the climatology, primes represent the anomalies of SIC and SIT, and A represents the area. We confirm that SIT anomalies provide approximately five times the absolute contribution to the interannual variability of SIV than SIC anomalies do (Extended Data Fig. 7).

Lagged correlation analysis with SIV and SIE

We calculate the lagged Pearson product moment correlation coefficient between 9–11-year time series of biweekly CryoSat-2 SIV and future daily pan-Arctic SIE from OSI-450, up to a maximum lead time of 365 days. Only the SIV observations from outside the NSIDC MASIE Central Arctic region[71] are used for these calculations because the Central Arctic was perennially sea-ice covered over our study period. (It is important to note that this region should be included in a similar analysis if the Central Arctic sea-ice coverage varies between seasons, for instance, in a model analysis of future SIV and SIE fields.) We compare this to lagged correlations between biweekly SIE and future daily SIE. Only 1 of the 24 biweekly (that is, twice monthly for a year) pan-Arctic SIV fields, and 6 of the 24 SIE fields, exhibit statistically significant ($P < 0.05$) trends over the 2011–2020 study period. Therefore, we show correlations without detrending in the main text but repeat the same analysis with detrended time series in Extended Data Fig. 8. The given P values for correlations are based on an F test. Although SIE is available daily, SIV is available at biweekly intervals, so correlations can be obtained for only select lead day–target day pairs. To visualize the correlation maps, we use a two-dimensional median filter (with a radius of 21 days) to interpolate between gaps. Correlation maps for eight regions based on the MASIE definitions[71] are also shown in Extended Data Fig. 9.

Significant correlations can be obtained between the 'radar freeboard volume' (the original uncorrected CryoSat-2 radar freeboards multiplied by the sea-ice area) and the future pan-Arctic SIE. However, replacing corrected SIV (Fig. 3a) with uncorrected radar freeboard volume results in approximately half the increase in lead time of skilful September sea-ice forecasts, versus the reference forecast using SIE (Fig. 3b). This emphasizes the importance of the freeboard-to-thickness conversion in summer (freeboard bias correction and impact of snow load) and in winter (impact of snow load only) for improving seasonal predictions.

A bootstrapping approach is used to assess the robustness of correlations. The correlations cover a period of 9–11 years depending on the availability of CryoSat-2 observations for a certain target day and lead time. Therefore, the above analysis is repeated 100 times but randomly sampling all but one year of the 9–11-year time series, with replacement, to determine the standard deviation (variability) of the correlations. In Extended Data Fig. 10, the variability of the 100 recalculated correlation coefficients provides a measure of the robustness of the patterns identified in Fig. 3. Extended Data Fig. 10 also shows the same bootstrapping analysis for the detrended correlation maps in Extended Data Fig. 8. For the regions of SIE correlations at lead times of up to 3 months, using either SIV or SIE, the standard deviations of the bootstrapped correlations are generally <0.06 (and <0.04 for target days in September). However, the re-emergence region of sea-ice correlations for SIV leading SIE, at 100–280 days for target days in October–November, produces standard deviations on the bootstrapped correlations of 0.06–0.10 (Extended Data Fig. 10). We require a longer consistent time series of SIT observations to more robustly validate this re-emergence region of correlations based on SIV anomalies.

Data availability

ESA Level-2 Baseline-D CryoSat-2 observations for May–September 2011–2020 from the ESA GPOD SARvatore and SARInvatore services were publicly available online for the initial manuscript submission but have since been removed. Please contact the corresponding author directly for access to these data. The dataset of samples for training and testing the CNN classification algorithm for CryoSat-2 is available from https://doi.org/10.1016/j.rse.2021.112744[7]. Daily observations of sea-ice drift are available from the NSIDC Polar Pathfinder dataset at https://nsidc.org/data/nsidc-0116/versions/4[43]. Remotely sensed observations of melt-pond fraction are available from the Sentinel-3 OLCI sensor through the University of Bremen at https://seaice.uni-bremen.de/melt-ponds/[54]. Snow depth and density estimates from SnowModel-LG are available from NSIDC at https://doi.org/10.5067/27A0P5M6LZBI[25]. Weekly 12.5-km estimates of the sea-ice age are available from the Version 4 product at NSIDC at https://nsidc.org/data/nsidc-0611[43]. The Airborne EM dataset includes observations from the AWI RV *Polarstern* ARK-XXVI/3 TransArc campaign in 2011[64], available from https://doi.org/10.1594/PANGAEA.937197, and the IceBird campaigns from 2016 to 2018[22]. Daily ULS sea-ice draft observations from BGEP moorings A, B and D are available from https://www.whoi.edu/beaufortgyre for the period between 2011 and 2018. Daily ULS and ADCP ice draft observations from five moorings in the Laptev Sea for 2010 to 2016 are publicly available from https://doi.org/10.1594/PANGAEA.899275 and https://doi.org/10.1594/PANGAEA.912927. Monthly ULS ice draft observations from four moorings in Fram Strait between 2010 and 2018 are publicly available from https://doi.org/10.21334/npolar.2021.5b717274. SIC is available from the OSISAF 'OSI-450' climate data record at https://osi-saf.eumetsat.int/products/osi-450[70]. Reanalysed model estimates of SIV are available from the Applied Physics Laboratory Version 2.1 reprocessed PIOMAS[8,30] at http://psc.apl.uw.edu/research/projects/arctic-sea-ice-volume-anomaly/data/model_grid. The final pan-Arctic CryoSat-2 SIT data spanning October 2010 to July 2020 are available from the British Antarctic Survey Polar Data Centre at https://doi.org/10.5285/D8C66670-57AD-44FC-8FEF-942A46734ECB.

Code availability

The MATLAB FBEM for simulating the backscattered SAR altimeter waveform from snow-covered sea ice, including an option for simulating waveforms from melt-pond-covered sea ice, is publicly available at https://doi.org/10.5281/zenodo.6554740. The look-up table for the EM bias correction is available at https://doi.org/10.5281/zenodo.6558485. The code for converting CryoSat-2 radar freeboards to thickness is available at https://doi.org/10.5281/zenodo.6558483.

44. Wingham, D. J. et al. CryoSat: a mission to determine the fluctuations in Earth's land and marine ice fields. *Adv. Space Res.* **37**, 841–871 (2006).
45. Dinardo, S. et al. Coastal SAR and PLRM altimetry in german bight and west baltic sea. *Adv. Space Sci.* **62**, 1371–1404 (2018).
46. Landy, J. C., Tsamados, M. & Scharien, R. K. A facet-based numerical model for simulating SAR altimeter echoes from heterogeneous sea ice surfaces. *IEEE Trans. Geosci. Remote Sens.* **57**, 4164–4180 (2019).
47. Kurtz, N. T., Galin, N. & Studinger, M. An improved CryoSat-2 sea ice freeboard retrieval algorithm through the use of waveform fitting. *Cryosphere* **8**, 1217–1237 (2014).
48. Polashenski, C., Perovich, D. & Courville, Z. The mechanisms of sea ice melt pond formation and evolution. *J. Geophys. Res.* **117**, C01001 (2012).
49. Fetterer, F. M., Drinkwater, M. R., Jezek, K. C., Laxon, S. W. & Onstott, R. G. in *Microwave Remote Sensing of Sea Ice* (ed. Carsey, F.) 111–135 (American Geophysical Union, 1992).
50. Fung, A. K. & Chen, K. S. An update on the IEM surface backscattering model. *IEEE Geosci. Remote Sens. Lett.* **1**, 75–77 (2004).
51. Ray, C. et al. SAR altimeter backscattered waveform model. *IEEE Trans. Geosci. Remote Sens.* **53**, 911–919 (2015).
52. Ulaby, F. T., Moore, R. K. & Fung, A. K. *Microwave Remote Sensing: Active and Passive* (Artech House, 1982).
53. Scharien, R. K., Landy, J. & Barber, D. G. First-year sea ice melt pond fraction estimation from dual-polarisation C-band SAR–Part 1: In situ observations. *Cryosphere* **8**, 2147–2162 (2014).
54. Istomina, L. et al. Retrieval of sea ice surface melt using OLCI data onboard Sentinel-3. In *American Geophysical Union, Fall Meeting 2020* abstr. C017-07 (AGU, 2020).
55. Landy, J. C., Ehn, J. K. & Barber, D. G. Albedo feedback enhanced by smoother Arctic sea ice. *Geophys. Res. Lett.* **42**, 10714–10720 (2015).
56. Landy, J., Ehn, J., Shields, M. & Barber, D. Surface and melt pond evolution on landfast first-year sea ice in the Canadian Arctic Archipelago. *J. Geophys. Res.* **119**, 3054–3075 (2014).
57. Willatt, R. C., Giles, K. A., Laxon, S. W., Stone-Drake, L. & Worby, A. P. Field investigations of Ku-band radar penetration into snow cover on Antarctic sea ice. *IEEE Trans. Geosci. Remote Sens.* **48**, 365–372 (2009).
58. Willatt, R. et al. Ku-band radar penetration into snow cover on Arctic sea ice using airborne data. *Ann. Glaciol.* **52**, 197–205 (2011).
59. Nandan, V. et al. Effect of snow salinity on CryoSat-2 Arctic first-year sea ice freeboard measurements. *Geophys. Res. Lett.* **44**, 10419–10426 (2017).
60. Stroeve, J. et al. Surface-based Ku-and Ka-band polarimetric radar for sea ice studies. *Cryosphere* **14**, 4405–4426 (2020).
61. Mallett, R. D., Lawrence, I. R., Stroeve, J. C., Landy, J. C. & Tsamados, M. Brief communication: Conventional assumptions involving the speed of radar waves in snow introduce systematic underestimates to sea ice thickness and seasonal growth rate estimates. *Cryosphere* **14**, 251–260 (2020).
62. Alexandrov, V., Sandven, S., Wahlin, J. & Johannessen, O. M. The relation between sea ice thickness and freeboard in the Arctic. *Cryosphere* **4**, 373–380 (2010).
63. Ricker, R., Hendricks, S., Helm, V., Skourup, H. & Davidson, M. Sensitivity of CryoSat-2 Arctic sea-ice freeboard and thickness on radar-waveform interpretation. *Cryosphere* **8**, 1607–1622 (2014).
64. Hendricks, S. et al. Airborne sea ice plus snow thickness measurements during POLARSTERN campaign ARK-XXVI/3 (TransArc) in the Arctic Ocean. PANGAEA Alfred Wegener Institute, Helmholtz Centre for Polar and Marine Research (2012).
65. Pfaffling, A., Haas, C. & Reid, J. A direct helicopter EM sea ice thickness inversion, assessed with synthetic and field data. *Geophysics* **72**, 127–137 (2007).
66. Haas, C., Gerland, S., Eicken, H. & Miller, H. Comparison of sea-ice thickness measurements under summer and winter conditions in the Arctic using a small electromagnetic induction device. *Geophysics* **62**, 749–757 (1997).
67. Belter, H. J. et al. Satellite-based sea ice thickness changes in the Laptev Sea from 2002 to 2017: comparison to mooring observations. *Cryosphere* **14**, 2189–2203 (2020).
68. Krishfield, R. A. & Proshutinsky, A. *BGOS ULS Data Processing Procedure* Woods Hole Oceanographic Institute Report (WHOI, 2006).
69. Belter, H. J., Krumpen, T., Janout, M. A., Ross, E. & Haas, C. An adaptive approach to derive sea ice draft from upward-looking acoustic Doppler current profilers (ADCPs), validated by upward-looking sonar (ULS) data. *Remote Sens.* **13**, 4335 (2021).
70. Lavergne, T. et al. Version 2 of the EUMETSAT OSI SAF and ESA CCI sea-ice concentration climate data records. *Cryosphere* **13**, 49–78 (2019).
71. Fetterer, F., Savoie, M., Helfrich, S. & Clemente-Colón, P. *Multisensor Analyzed Sea Ice Extent - Northern Hemisphere (MASIE-NH), Version 1* (National Snow and Ice Data Centre, 2010).

Acknowledgements M.T., J.C.L., Y.A., G.J.D., J.C.S. and H.D.B.S.H. acknowledge financial support from the UKRI Natural Environment Research Council Project (NERC) 'PRE-MELT' under the split grant awards NE/T001399/1, NE/T000546/1 and NE/T000260/1. J.C.L. was also supported by the European Space Agency Living Planet Fellowship 'Arctic-SummIT' under grant ESA/4000125582/18/I-NS and the CIRFA project through the Research Council of Norway (RCN) under grant number 237906. D.G.B. acknowledges support from the Natural Sciences and Engineering Research Council of Canada (NSERC). M.T. and Y.A. acknowledge support from 'Towards a marginal Arctic sea ice cover' (NE/R000085/1). We thank the SARvatore (SAR Versatile Altimetric Toolkit for Ocean Research and Exploitation) service available through the ESA GPOD for providing Level-2 CryoSat-2 observations; and the WHOI Beaufort Gyre Exploration Programme and AWI IceBird Programme for providing essential observations for ground truthing new satellite datasets. ADCP and ULS moorings were deployed, recovered and processed within the framework of the Russian–German project CATS/Transdrift (grant 63A0028B) and QUARCCS (grant 03F0777A).

Author contributions J.C.L. conceived the study and managed the research. M.T., J.C.L. and Y.A. wrote the grant proposals that majority funded the study. J.C.L., G.J.D., J.C.S., S.E.L.H., T.K., H.J.B. and A.S.K. collected and prepared the raw data. J.C.L. and G.J.D. developed the methods and wrote the software. M.B. and J.C.L. designed the lagged correlation analyses. J.C.L. led the writing of the paper and produced the figures. All authors revised and improved the manuscript.

Competing interests The authors declare no competing interests.

Additional information

Supplementary information The online version contains supplementary material available at https://doi.org/10.1038/s41586-022-05058-5.

Correspondence and requests for materials should be addressed to Jack C. Landy.

Peer review information *Nature* thanks Sara Fleury and the other, anonymous, reviewer(s) for their contribution to the peer review of this work.

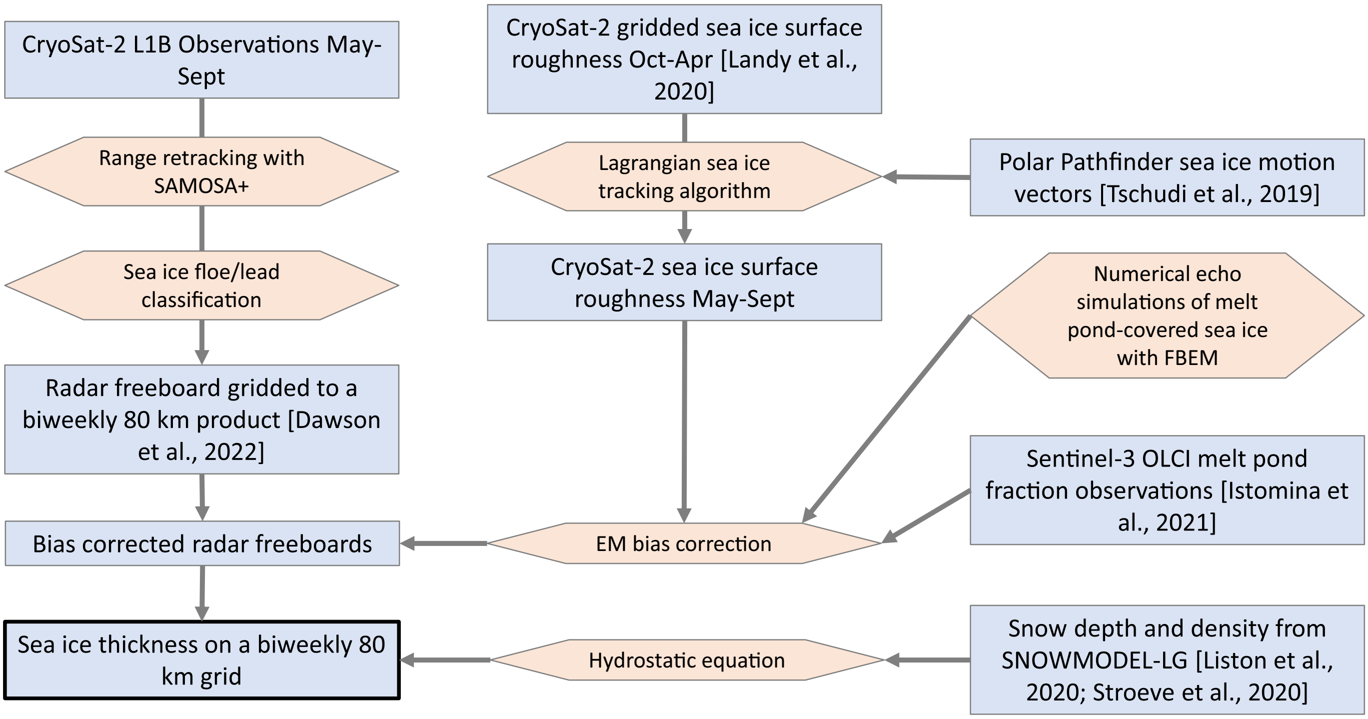

Extended Data Fig. 1 | Flow diagram of the CryoSat-2 summer sea ice thickness processing chain. CryoSat-2 data and auxiliary data products are shown in blue. Key processing steps are shown in orange.

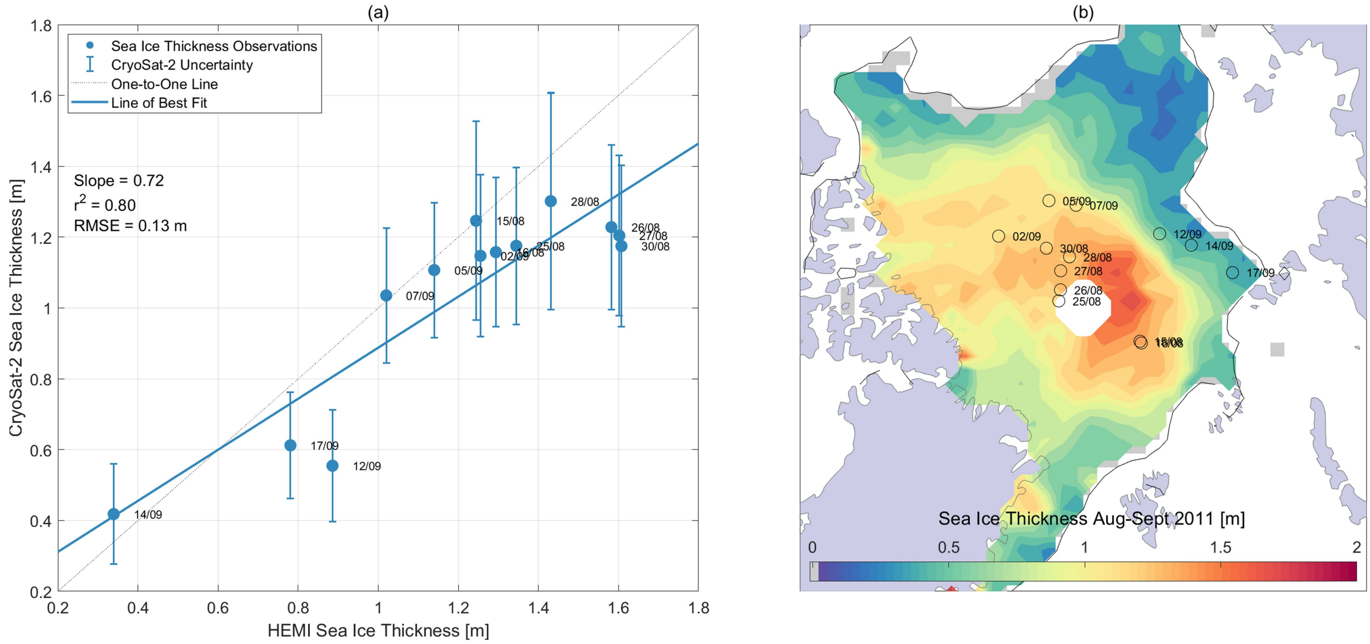

Extended Data Fig. 2 | CryoSat-2 sea ice thickness validation against airborne observations from the 2011 *TransArc* campaign of the AWI Polarstern Icebreaker. (a) Comparison of CryoSat-2 sea ice thickness observations with airborne EM thickness measurements. The AEM data were averaged to 80-km scale before comparing with CryoSat-2. The technique for deriving CryoSat-2 ice thickness uncertainties is described within the Methods section. (b) Map and dates of AEM sea ice thickness data collection overlaid on the CryoSat-2-derived sea ice thickness field for Aug 15th–Sept 15th 2011. Information on the SIT data available from *TransArc* can be found here https://doi.org/10.1594/PANGAEA.937197. Map in panel b produced using MATLAB code from ref. [42].

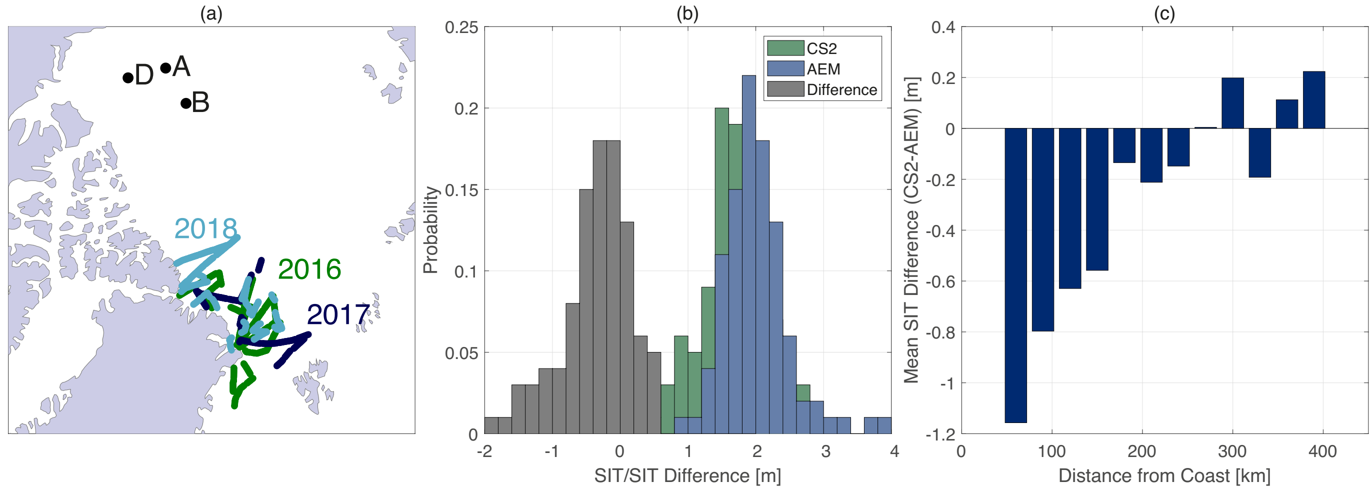

Extended Data Fig. 3 | CryoSat-2 sea ice thickness validation against airborne observations from the AWI *IceBird* Program 2016–2018. (a) Map of the airborne EM observations used for sea ice thickness validation. Three annotations in the Beaufort Sea mark the locations of the BGEP Moorings (see Extended Data Fig. 4). (b) Comparison of CryoSat-2 sea ice thickness observations with coinciding AEM measurements. The airborne data were averaged to 80-km scale before comparing with CryoSat-2. (c) Mean ice thickness difference between CryoSat-2 and the AEM as a function of the distance of observations from the coast. Map in panel a produced using MATLAB code from ref. [42].

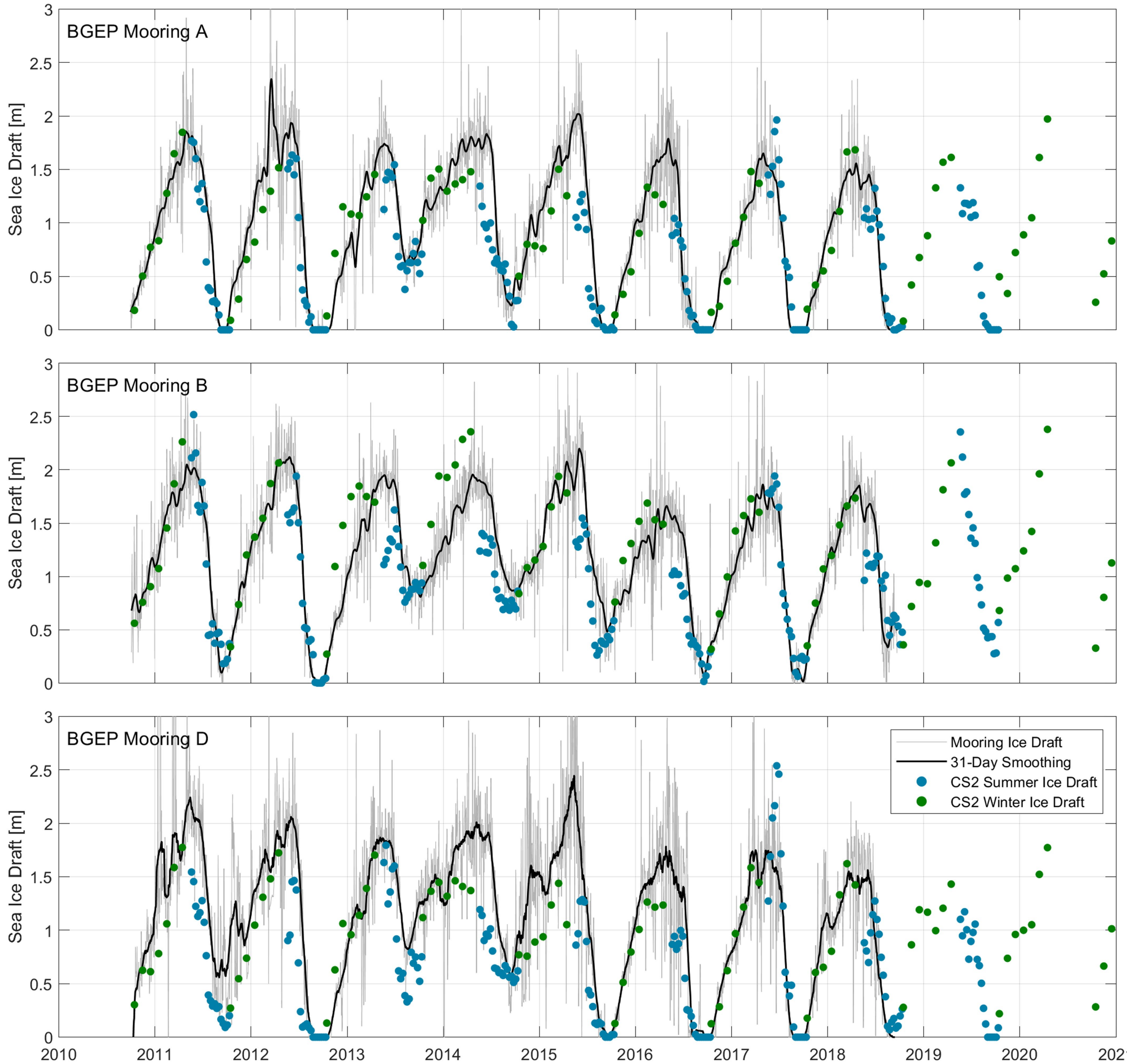

Extended Data Fig. 4 | Comparison of sea ice draft measured by the Beaufort Gyre Exploration Program (BGEP) Mooring Upward-Looking Sonar (ULS) sensors with ice draft estimates by CryoSat-2 in a 150 km radius surrounding each mooring. CryoSat-2 draft observations in winter (green points) use the LARM sea ice product (Landy, et al., 2020) and in summer (blue points) use the processing algorithm presented here. BGEP Mooring A is located at approximately 75N 150W, Mooring B at 78N 150W, and Mooring D at 74N 140W and are shown in Extended Data Fig. 3a. Information on the BGEP mooring ULS data can be found here https://www2.whoi.edu/site/beaufortgyre/data/mooring-data/.

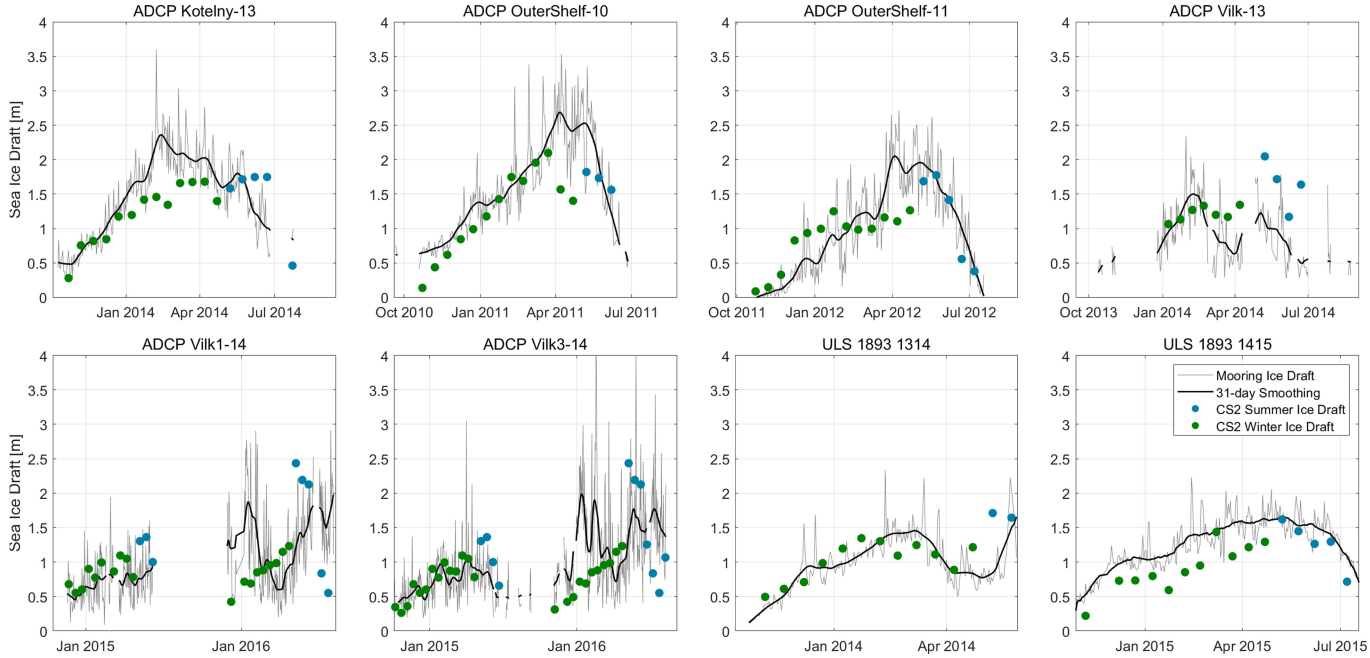

Extended Data Fig. 5 | Comparison of sea ice draft measured by moored Upward Looking Sonar (ULS) and Acoustic Doppler Current Profiler (ADCP) sensors in the Laptev Sea with ice draft estimates by CryoSat-2 in a 150 km radius surrounding each mooring. CryoSat-2 draft observations in winter (green points) use the LARM sea ice product (Landy, et al., 2020) and in summer (blue points) use the processing algorithm presented here. Locations and information for the ULS and ADCP sensors on Laptev Sea moorings can be found here https://doi.org/10.1594/PANGAEA.899275 and https://doi.org/10.1594/PANGAEA.912927 respectively.

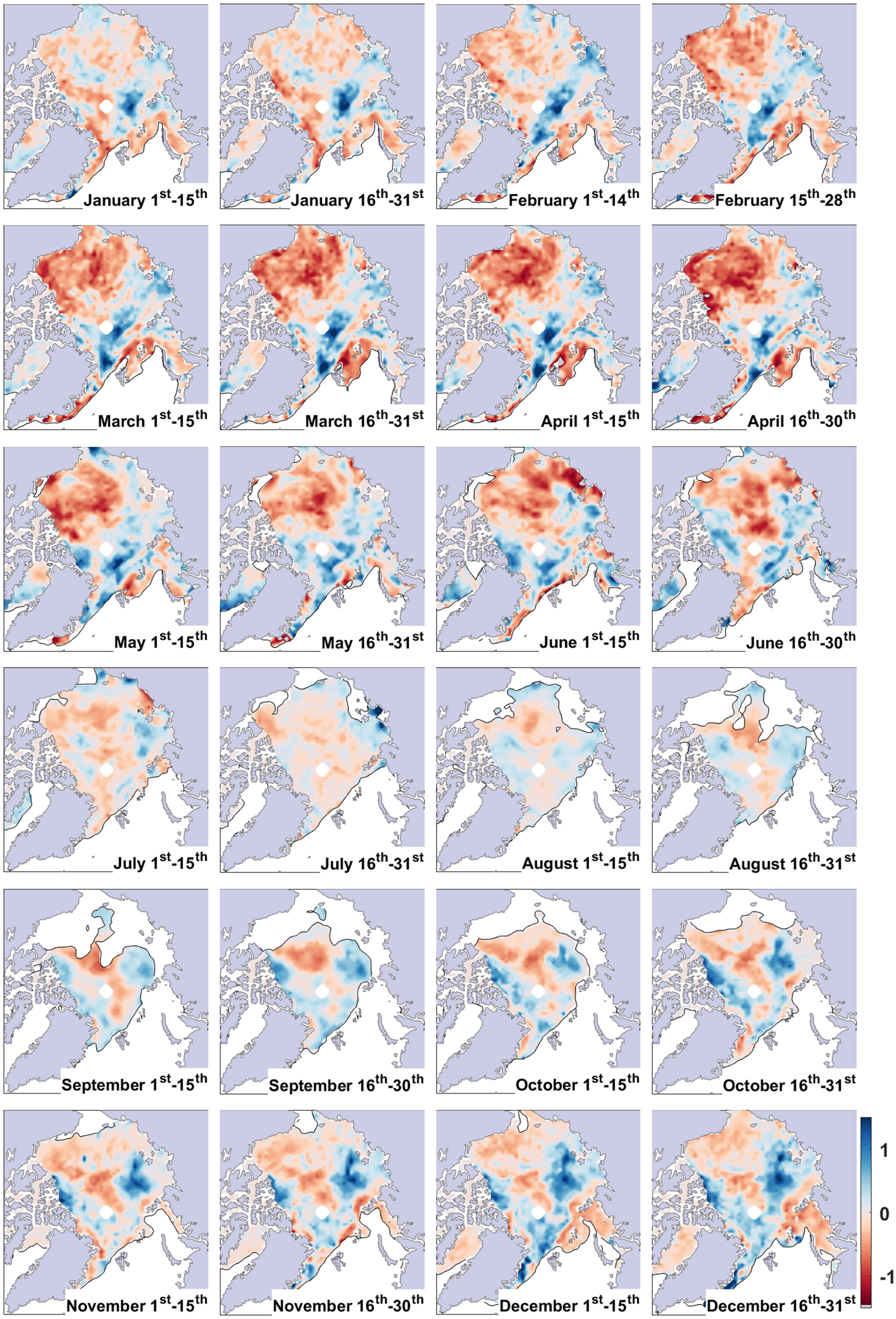

Extended Data Fig. 6 | Arctic sea ice thickness anomalies [m] measured over the entire year at biweekly intervals by CryoSat-2 in 2016, compared to the 2011–2020 average. Observations for October–April are obtained from the LARM algorithm (Landy, et al., 2020). Observations for May–September are obtained from the new method presented here. Black contours represent the sea ice extent (15% ice concentration edge). Maps produced using MATLAB code from ref. [42].

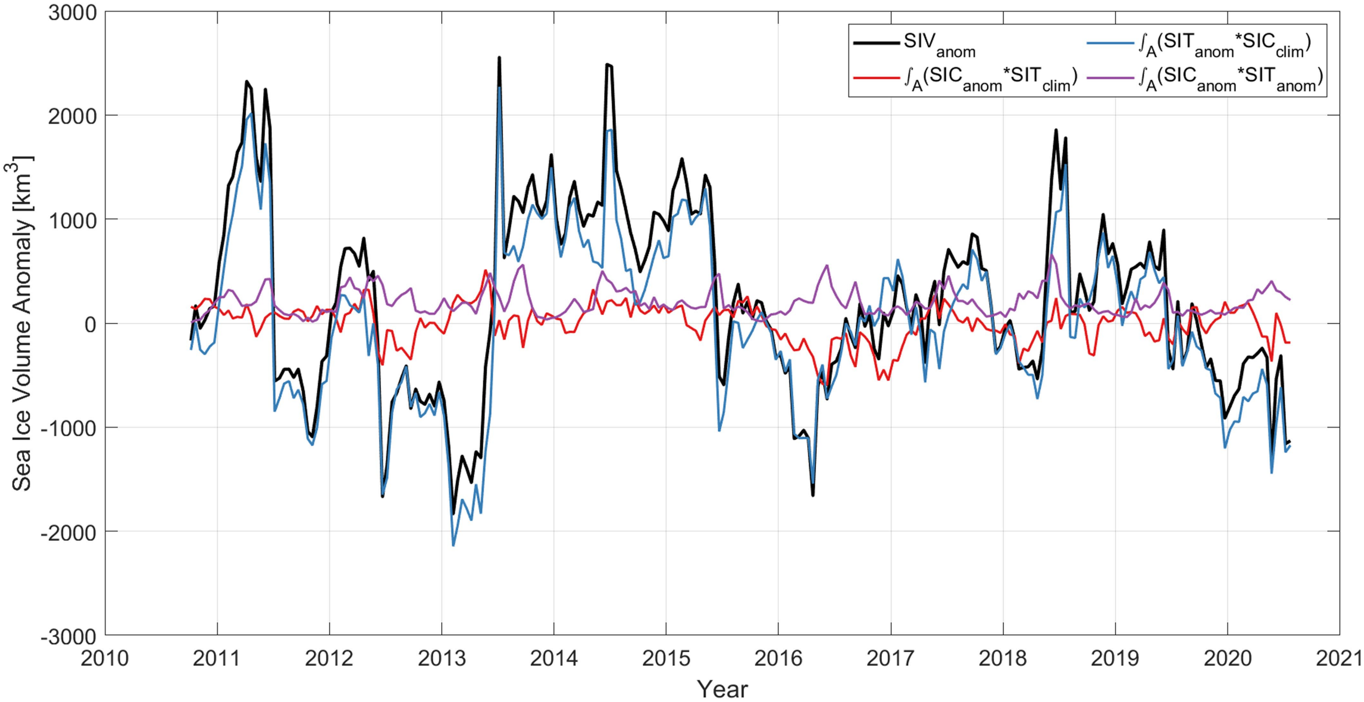

Extended Data Fig. 7 | Sea ice volume anomaly decomposition. In black, the SIV anomaly after removing the climatological seasonal cycle of SIV obtained from the 2010–2020 time series of SIV from CryoSat-2 SIT and OSISAF SIC. In red, blue, and purple are the contributions of SIC anomalies, SIT anomalies, and their correlated component, respectively, to the time series of SIV anomalies. The correlations between the anomalies of SIV with respective anomalies of SIT, SIC, and their correlated component, are 0.97, 0.27, and 0.21. SIT anomalies provide the dominant contribution to SIV interannual variability compared to SIC anomalies.

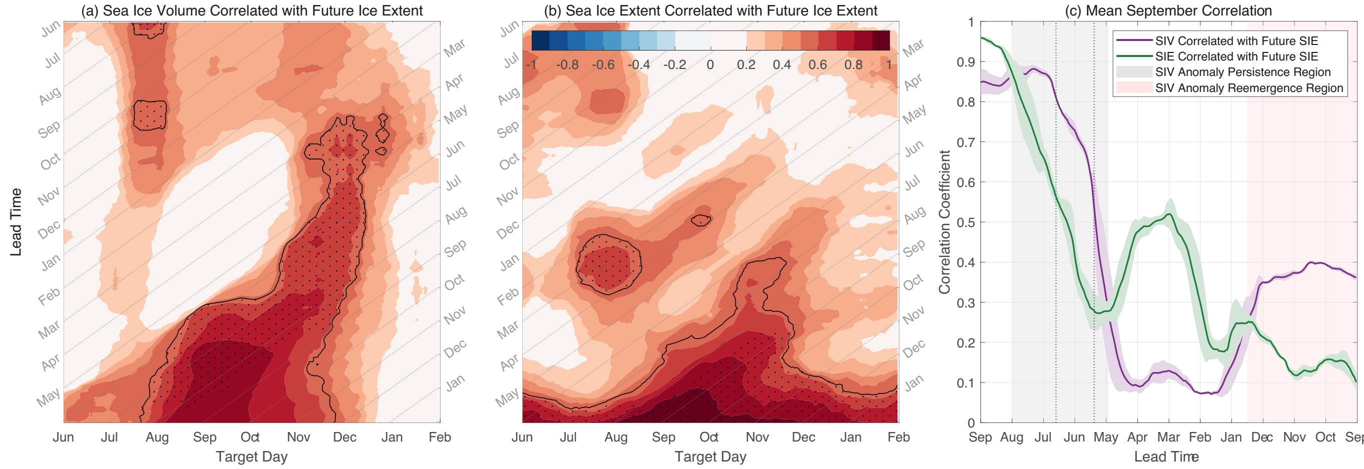

Extended Data Fig. 8 | Reproduction of the lag correlation plots in Fig. 3 of the main paper but with SIE and SIV time series linearly detrended before calculating the correlations. (a) Correlations between SIV and later SIE and (b) correlations between SIE and later SIE. Black lines mark correlations with a statistical significance of p = 0.1 and stippling marks where SIE->SIV correlations are higher than SIE->SIE for (a) or vice versa for (b). The grey lines mark lead times for each month as contours. (c) Mean (with standard deviation envelope) correlation for September SIE including two regions of predictability where SIV offers improvements over SIE.

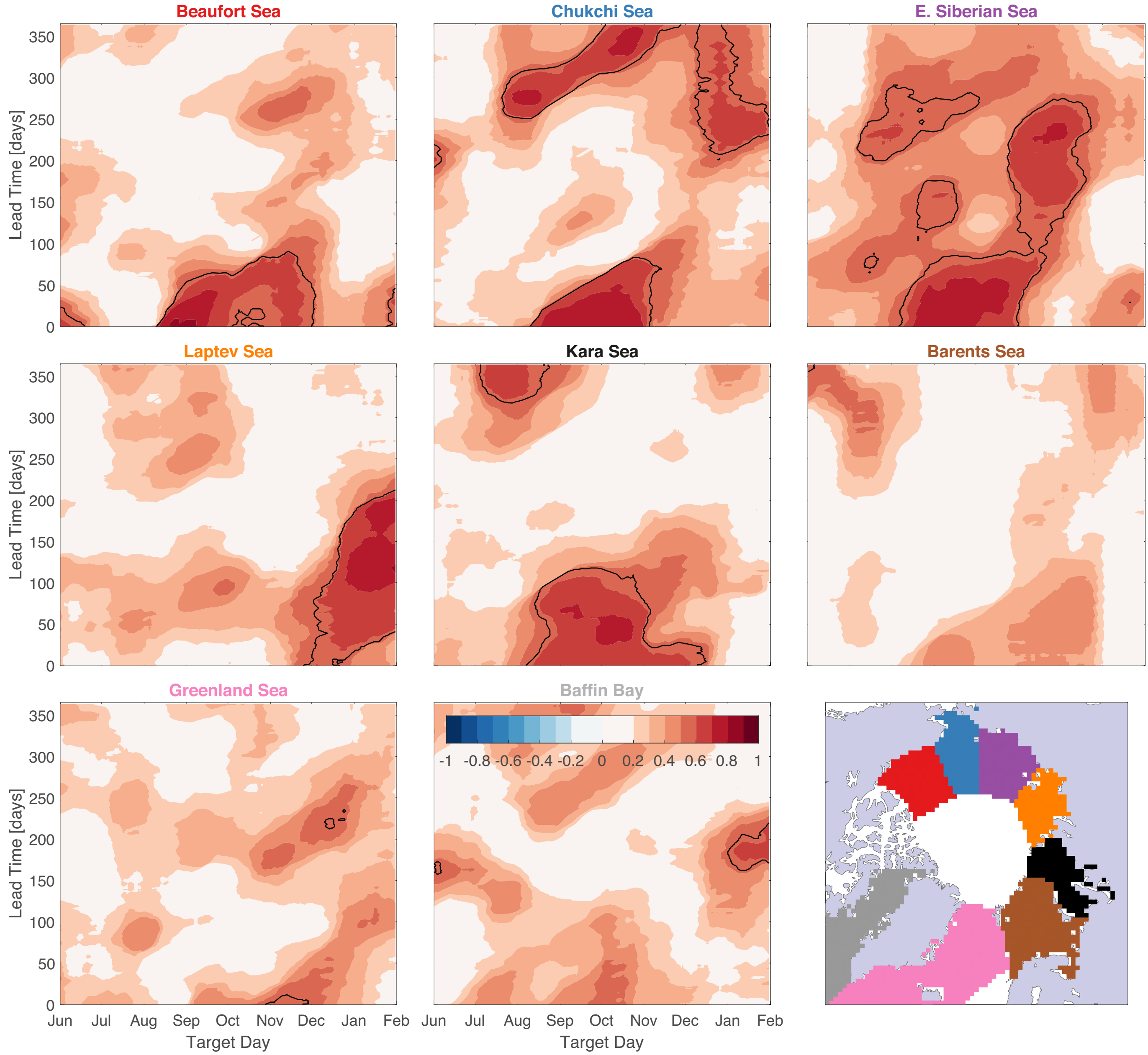

Extended Data Fig. 9 | Lag correlation plots between SIE and earlier SIV for different regions of the Arctic. The black lines mark correlations with a statistical significance of p = 0.1 and regions are defined by the NSIDC *MASIE* system, as displayed on the map. The Central Arctic Ocean region, referred to in the main text, is shown in white between the marginal Arctic seas. Map in the bottom-right panel produced using MATLAB code from ref. [42].

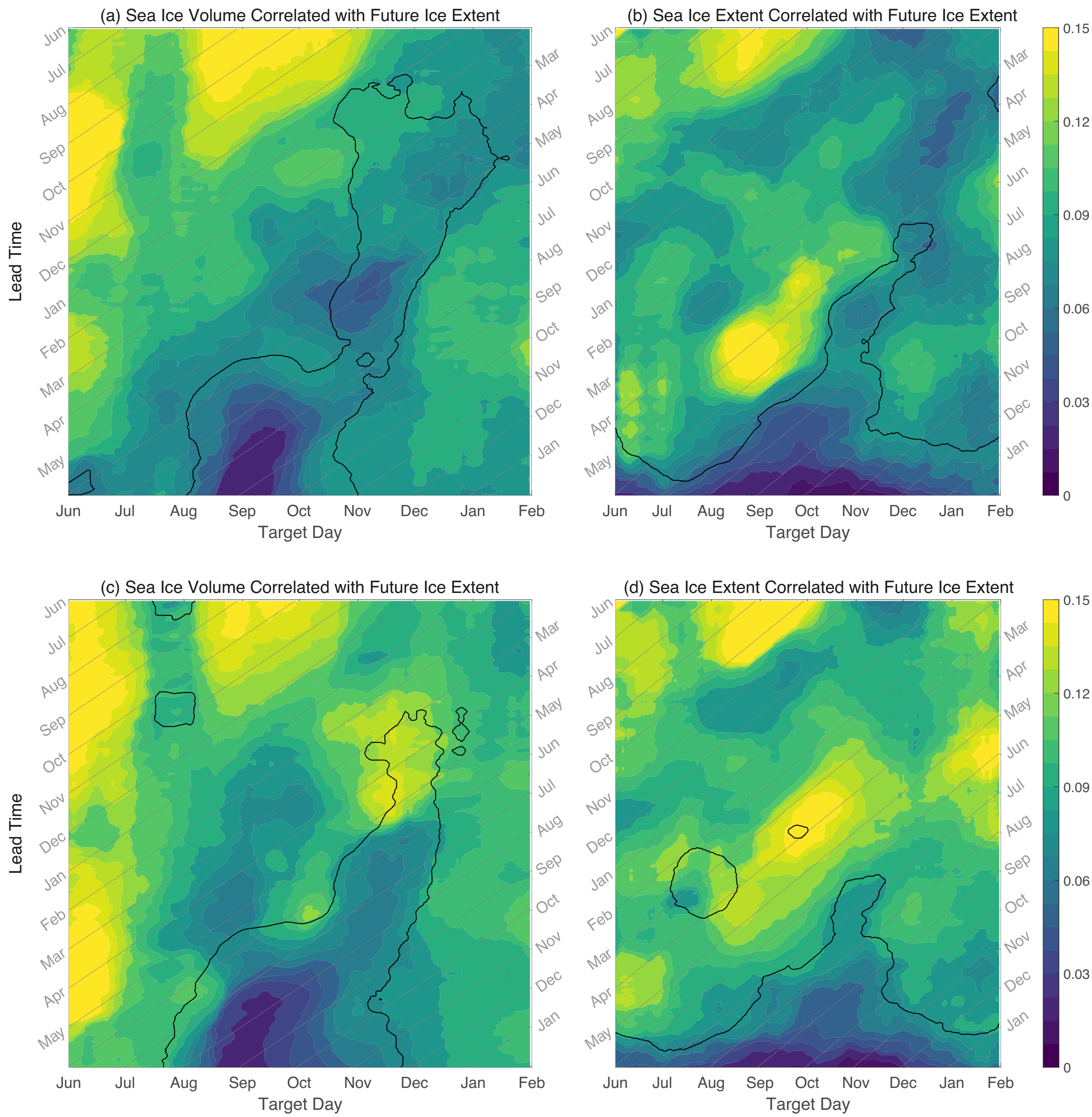

Extended Data Fig. 10 | Standard deviations on bootstrapped correlation coefficients between SIV leading SIE and SIE leading SIE. Correlations are recalculated 100 times but each time randomly sampling N minus 1 of the 9–11-year time series available from, CryoSat-2, with replacement, so that one pair of observations is excluded from the calculation. The variability of the 100 recalculated correlation coefficients provides a measure of the robustness of the patterns identified in Fig. 3 of the main text (top row) and Extended Data Fig. 7 (bottom row), i.e., with and without detrending time series, respectively. Black lines show contours of $p = 0.1$ from the correlation plots in Fig. 3 in the main text (top row) and Extended Data Fig. 7 (bottom row).